Chromospheric Microjets in the Penumbra of a Sunspot

Master Thesis

Ainar Drews
Institute of Theoretical Astrophysics
University of Oslo

ABSTRACT

In this thesis chromospheric features called Penumbral Microjets (PMJs) are investigated in a sunspot. Observations of high resolution in space, time and wavelength from the Swedish 1-meter Solar Telescope (SST) are used to probe the Ca II 8542 Å -line. The goal is to obtain detailed spectral signatures of PMJs in the Ca II 8542 Å -line, as well as basic statistical measures such as lifetime and sizes. This is achieved by the implementation of an automated detection scheme employing dimensionality reduction methods and a simple learning algorithm which together reduce and classify the observations from the SST. The advantages of employing an automated numerical detection scheme are exploited to assemble a large sample of objects and extract statistically significant results from it. The obtained statistical values and spectra are then discussed and put in a wider context.

ACKNOWLEDGEMENTS

For enabling me to have this wonderful, albeit at times frustrating learning experience with long hours spent sifting through code and staring at grey-on-grey pixels, I would first like to thank my two supervisors, Luc Rouppe von der Voort and Mats Carlsson.

I thank them both both for the opportunity to work on a project I was quite free to formulate myself, and their continual support when I needed them.

Furthermore I would like to thank my family for their good cheer and reminders to maybe look at the sun outdoors once in a while. Lastly, I want to thank Marianne Steinkjer for her continued support and motivation, and putting up with the high piles of encrusted coffee cups and dirty dishes I nested in towards the end of this thesis.

CONTENTS

Abstract **3**

Acknowledgements **5**

1 INTRODUCTION **9**
1.1 Background, motivations and goals . . . 9
1.2 Layout of the Thesis . . . 12

2 The Sun **13**
2.1 The solar atmosphere . . . 13
2.1.1 The photosphere . . . 14
2.1.2 The chromosphere . . . 15
2.1.3 The Corona (and the transition region) . . . 15
2.2 Sunspots . . . 16

3 The Observations **19**
3.1 The Swedish 1-m Solar Telescope . . . 19
3.1.1 The Tower and Turret . . . 19
3.1.2 Adaptive Optics . . . 23
3.1.3 CRISP . . . 23
3.1.4 Blue Beam . . . 27
3.2 Comments on Seeing . . . 28
3.3 MOMFBD . . . 29
3.4 Post processing of observations . . . 30
3.5 The Datasets of 28-June-2010 . . . 31

4 Penumbral Microjets **39**
4.1 Penumbral Microjets in the literature . . . 39
4.2 Notes on observing PMJs in Ca II 8542 Å . . . 43
4.3 Motivations and areas of interest . . . 45

5 Methods **47**
5.1 Pipeline Overview . . . 47
5.2 Normalisation of the data set . . . 48
5.3 Principal Component Analysis . . . 50
5.3.1 PCA: Introduction and Motivation . . . 50
5.3.2 Mathematical and Computational implementation of Principle Component Analysis 52
5.3.3 PCA performed on the present observations, and selection of Principle Components 55
5.4 The k-Nearest Neighbour Algorithm . . . 59
5.4.1 Implementation of the k-NN algorithm . . . 60
5.4.2 Reference set assembly . . . 61
5.4.3 k-selection for the k-NN algorithm . . . 63
5.5 Object tracking and statistical analysis . . . 64

6 Results **67**
6.1 Appearance and reasonability of detections . . . 67
6.1.1 General discussion of the detections . . . 67
6.1.2 The Halo effect . . . 70
6.2 The line profile of PMJs in the Ca II 8542 Å -line . . . 71
6.3 PMJ lifetimes and morphology . . . 74
6.3.1 Presentation of statistical measures . . . 74
6.3.2 Comparison and discussion of found statistical values . . . 79
6.4 PMJs in the Ca II 8542 Å -line viewed in the Ca II H-line . . . 83

7 Conclusion and Outlook **85**

CHAPTER 1

INTRODUCTION

1.1 Background, motivations and goals

Penumbral Microjets (PMJs) are transient objects found in the cromospheric penumbra of sunspots. These objects have previously been described as small jet-like phenomena with a lifetime of approximately 60 seconds and dimensions of about 400 km $\times(1000 - 4000)$ km (Katsukawa et al. (2007) and Jurčák & Katsukawa (2008)). It has been speculated that PMJs are caused by magnetic reconnection. Magnetic reconnection is an interesting physical process that may in part explain the high temperatures of the solar corona, albeit at larger scales. This means that PMJs may contribute to the understanding of magnetic reconnection at small scales, which may prove valuable when in turn considering larger scales.

PMJs have only relatively recently been observed and described for the first time, as a combination of high resolution and short cadences in observations is necessary to detect them at all. The required resolutions and cadence requirements necessary to observe have previously not been met, until newer generation telescopes became operational. Further, even though the theoretical diffraction limited resolutions may have been sufficient to detect PMJs from earth in the past, atmospheric distortions are an ever-present hindrance to achieve optimal resolutions. Therefore, it comes as no surprise that these small and short-lived objects were first discovered using the Solar Optical Telescope (SOT) onboard the Hinode spacecraft (Tsuneta et al. 2008), which has a high-quality optical setup with short possible exposures, and is furthermore unhindered by atmospheric distortions.

However, as PMJs are a recently discovered class of objects, observational, theoretical and numerical studies on the subject-matter are necessarily scarce. Previous observations and descriptions of PMJs have also been limited to the use of a relatively wide-band interference filter centered around the CaII H-line, and therefore no spectral signatures in any line have been put forth. G-band co-observations have also been used in further analysis of PMJs, but the events themselves have only been described in the Ca II H-line. Furthermore, detections and descriptions of PMJs have so far been performed manually, and the sample sizes for statistical analyses are therefore relatively limited.

The scarcity of literature, the lack of observations with high spectral resolutions, and the limited statistical studies are all direct motivators for the present work and the methods applied in it.

The observations used in this work are obtained from the Swedish 1-m Solar Telescope (SST) on La Palma (Scharmer et al. 2003a). Observations from the SST are unique in that the spatial, temporal and spectral parameters are all captured in high resolution *simultaneously*. Most commonly, observations from other comparable telescopes or instruments in use today routinely compromise one or more of these parameters to achieve a high-grade resolution in just the remaining. In contrast, the SST manages to deliver a high resolution in all of these three parameters. These resolutions can compete with, or are of similar grade, as those from other observatories that however do not provide high resolution in all these parameters simultaneously. As an example, the Solar Optical Telescope (SOT) on the Hinode spacecraft (Tsuneta et al. 2008), that as mentioned first discovered PMJs, achieves comparable spatial and temporal resolutions, but is not able to offer the high spectral resolution around chosen lines as the SST does. On the other hand the SOT is able to make long, continuous observations not affected by seeing. In short, the combination of high resolutions in several parameters makes the SST observations extremely well suited for in-depth analysis of solar features, which can be very dynamic in all parameters.

In this work, such observations are analysed using numerical methods of data-analysis and classification to detect PMJs automatically. The goal is to obtain significant and detailed statistical measures on PMJs. These should specifically encompass spectral properties, which the observations from the SST are well suited to uncover, as opposed to observations from earlier work. Furthermore, basic measures of lifetime, morphology, spatial distributions and dynamics shall be investigated and verified.

The numerical automation of PMJ detections is meant to increase the feasible sample sizes for extraction of statistical data, and is meant to yield a significant underpinning to derived properties and place them on a sure footing. Additionally, the automation of the detection process is also meant to limit the bias that is inherent in the manual selection of objects for analysis.

The automation scheme used here also stands in contrast to many detection schemes commonly used. Many of these schemes only consider relative intensity values, employing some sort of thresholding in one, or a few, spectral positions to identify objects. A recent example that employs such a scheme is Nelson et al. (2013), in which Ellerman Bombs are studied. As such approaches hinge on the very specific selection of threshold values and are liable to complications when considering variations in the average intensity across the field-of-view, the introduced bias and error-margin may be improved upon. Furthermore, objects on the sun are often characterised by characteristic spectral signatures that can be used as an identifying property, as well as an aid for analysis, yielding great motivation for a detection scheme involving more spectral measurements. Threshold values in one or few spectral positions on the other hand will be dependent on the specific data set, and values will not readily be transferable to other observations. In contrast, spectral signatures/shapes may in principle be transferable to observations in the same wavelengths and with similar spectral resolutions, while also yielding theoretical insight in themselves.

The present automated detection scheme and pre-analysis both neatly exploit the high spectral resolution of the present observations. The detection scheme also virtually directly offers information on the spectral signature of PMJs. This is made possible by using the well known multi-variable analysis tool of Principal Component Analysis (PCA) (succinctly summarised in Shlens (2005)), followed by the application of the multivariate object-recognition algorithm dubbed the k-Nearest-Neighbour (k-NN) algorithm (the k-NN algorithm is a well established algorithm, mentioned in many papers - an example of the algorithm is given in Guo et al. (2004), discussing the base algorithm, as well as a methods to improve it, a more comparative text is given in Yang & Liu (1999), which compares the k-NN algorithm to other classifiers in the context of text recognition). After the raw detections are performed, they are first cleaned

of noise, and further selection criteria are applied. Subsequently, objects are labelled and tracked through space and time, and secondary properties are derived. These include lifetimes and morphology.

Principle Component Analysis is both a tool for high-dimensionality data analysis, as well as a tool for the reduction of a data set to fewer dimensions. PCA is based on the study of the interdependence of covariances between different variables/dimensions in a data set, and quantifies these. Furthermore, PCA is used to reorder the data set along new dimensions which are no longer dependent. This allows for the selection of so called Principal Components in the new transformed data set, that describe the original data sufficiently well without significant data loss. PCA often precedes further study of high-dimensional data sets, and its uses are usually threefold. Firstly, PCA is commonly utilised as a primary means of analysis (covariance dependencies between dimensions). Subsequently it is often used as a method for reducing redundancy and noise in data. Lastly PCA is employed as a dimensionality reduction tool. The last step both simplifies the further numerical study of the data in terms of workload and computing time, but also in analytical terms of further comparative studies. Here, high-dimensional data often causes problems of non-uniqueness of data points, such as the 'curse of dimensionality' which is encountered in high-dimensional data analysis (a detailed discussion of this topic is carried out in Houle et al. (2010), specifically in the context of similarity measures). In the present context, the dimensions that are studied and reduced using PCA are the spectral intensity positions in the observational data from the SST, quantifying their dependencies, and reordering and reducing the data set according to the Principal Components.

The k-NN algorithm is a robust detection algorithm for multi-dimensional data, and is often called the simplest of the learning algorithms. The algorithm is based on the rather simple idea of comparing a data set that is to be classified, to a reference set of pre-classified objects. By comparing data points between sets, using some measure of similarity, unclassified points are classified according to their relative similarity to entries in the reference set. The k-NN algorithm's strength lies in its simplicity, and it is surprisingly resilient and effective. Furthermore, the k-NN algorithm is in wide use in a variety of fields, and has proven itself as a valuable tool for signal detection in a myriad of settings, examples including facial recognition, machine reading and voice recognition, and so it is well documented. The k-NN algorithm is robust, but can experience failure if the data analysed has too many dimensions. In this case, the 'curse of dimensionality' may be encountered, which is naturally preferably avoided. This, and computational work-cost is the motivation of the PCA reduction mentioned above. Thus the data set analysed by the k-NN algorithm will be the data set aligned along selected Principal Components found in the Principal Component Analysis.

Following the completion of initial classification of all data points in the observations, the classifications are then cleaned of dubious classifications and noise, using appropriate selection criteria, such as excluding detections of minute size and lifetimes and specifying a region of interest (such as the penumbra). The remaining objects are then tracked and labelled, and can be further analysed. These objects can again be tested for reasonability, excluding objects of unreasonable sizes and shapes (using automatic geometric fitting), all the while being careful not to introduce a new inherent bias that the automatic detection scheme was initially devised to avoid. This entire pipeline is discussed in detail throughout Chapter 5.

1.2 Layout of the Thesis

This thesis is organised in a manner that hopefully first gives the reader the necessary background in the material discussed. It then moves on to the methods used in this thesis, attempting to elucidate how they work and why they are utilised in the first place. Finally it arrives at the subsequent results produced and discusses these.

Thus we begin by inspecting the broader context of our study, the sun and its atmosphere as well as sunspots in Chapter 2. We then examine the observations used throughout this thesis, how they are obtained, and by what instruments in Chapter 3. The main focus of this thesis, Penumbral Microjets, are reviewed and the specific goals in studying them are reviewed and explained in Chapter 4. A large part of this thesis' work is concentrated in its constituent methods, which are discussed in Chapter 5. We then turn to the results of the thesis, which are presented in Chapter 6. Lastly, Chapter 7 seeks to discuss interesting avenues of further study as motivated by the preceding work and results presented.

To some degree the use of some observations in this work require justification and therefore analysis and explanation in their own right in order to place the subsequent main scientific results on a sure footing. These analyses however yield some scientific insights themselves, but must necessarily be presented before the final results. Further, some justification of the employed methods is also in order, which will also entail some preliminary analysis which may be seen as scientific results onto themselves, which again however precede the main results. Such results and deliberations are thus presented in the relevant chapters, alongside their relevant subject matter. These results may then be referenced and expanded on in the context of the main results presented towards the end of the text.

CHAPTER 2

THE SUN

The sun is our convenient stellar model laboratory and is a nicely average main sequence star, well suited for extrapolation and quite representative for a wide range of stars. Forgoing an in-depth treatment of solar dynamics and the standard solar model, a brief description of the solar atmosphere is given below, as the work presented here focuses on atmospheric phenomena on the sun.

2.1 The solar atmosphere

The sun has an atmosphere characterised by different temperatures, densities, atomic populations and strongly varying dynamics. The atmosphere of the sun is commonly divided into three parts; the photosphere, chromosphere and the corona, ordered outwards from the solar surface as given. These parts differ in temperature, density, composition and opacity.

The different values for the solar atmosphere mentioned below are taken from Carroll & Ostlie (2007) if not stated otherwise.

A schematic overview of the solar atmosphere is given in Figure 2.1, reproduced from Sekse (2013) (based on the original first given in Vernazza et al. (1981)), showing the atmospheric temperature stratification profile of the sun for the classic VAL3C model.

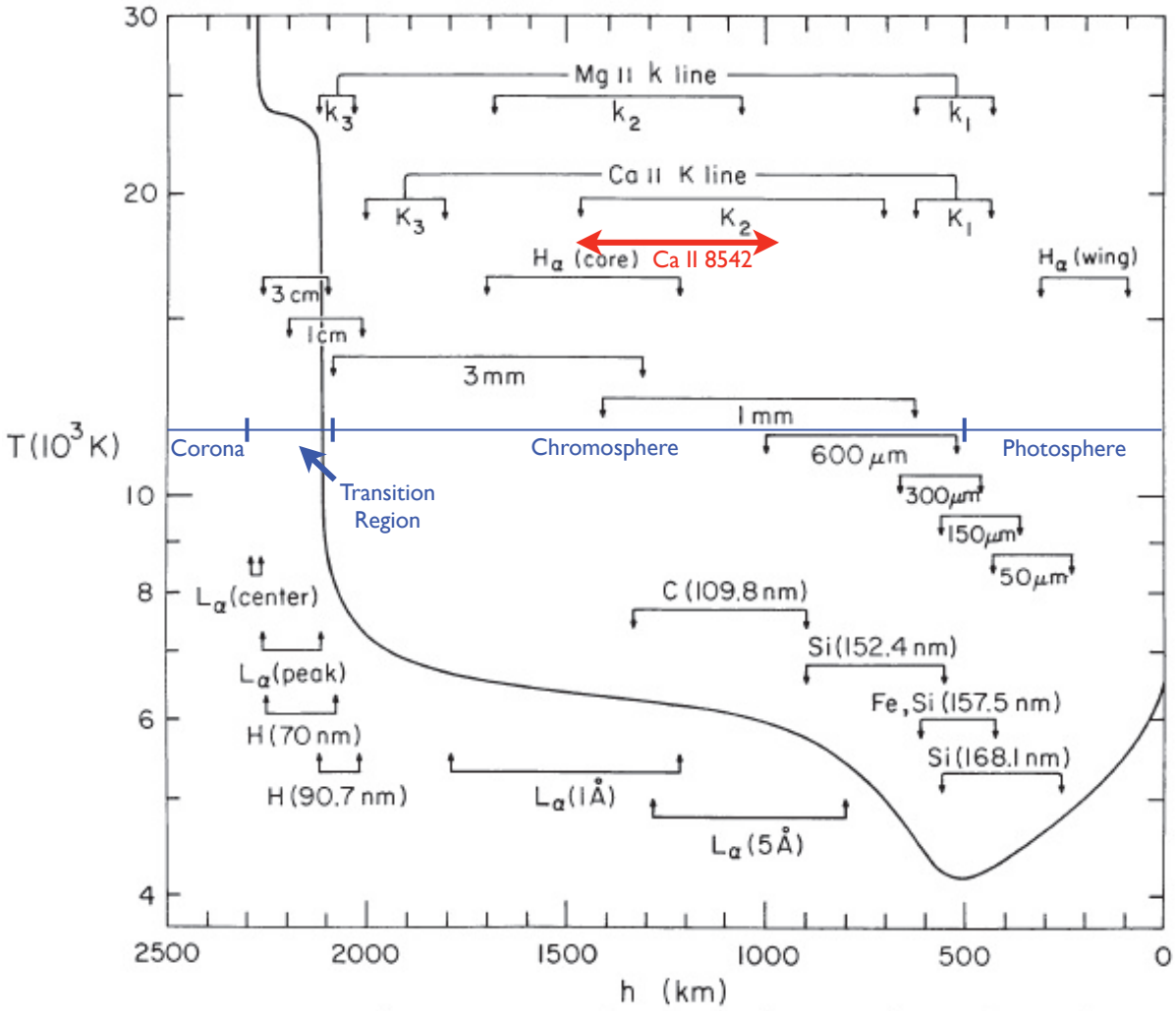

Figure 2.1: Schematic of the VAL3C model, depicting the temperature profile of the Sun with height, together with the approximate formation heights of various commonly used spectral lines, with the formation height of the Ca II 8542 Å -line and the different atmospheric boundaries highlighted. Reproduced from Sekse (2013).

2.1.1 The photosphere

The photosphere is the innermost part of the solar atmosphere, and its lower bound is meant to correspond to the sharp edge of the sun observable by eye in the visible wavelengths. It is thus the layer of the sun from which most of the visible light originates.

The photosphere is defined to begin at about 100 km *below* the height at which the optical depth of 500 nm light is unity ($\tau_{500} = 1$), which is the commonly defined origin-height of the solar atmosphere. At the lower edge of the photosphere, the optical depth of 500 nm light is $\tau_{500} \approx 23.6$, and the temperature is $T \approx 9400$K, with the temperature decreasing upwards.

The solar atmosphere experiences a local minimum in temperature at approximately 525 km height, which is above the $\tau_{500} = 1$ height. This minimum is used to define the upper bound of the photosphere. Above this height, the temperature begins to rise again, and the chromosphere is conveniently defined to begin. For the clarity of the temperature description, the reader is directed to Figure 2.1.

The visual appearance of the photosphere is mostly characterised by solar granulation. Solar granulation is the result of convection reaching up into the photosphere, the granules being the top of the convection zone. A granule appears as a bright blob with a darker border. Granules have a typical cross-section of 700 km. The brighter centers of granules correspond to upward flowing plasma, which subsequently cools itself in the optically thinner photosphere by radiating away photons. This cooling in turn causes a downflow that is channelled into the borders between granules, known as intergranular lanes. Granules have a lifetime of about $5 - 10$ min, corresponding to the time a convective bubble spends to rise and fall, and flow-velocities of about 0.4 km/s.

Striking features visible in the photosphere are sunspots, darker areas significantly larger than the solar granules. Sunspots have sizes of up to 30 000 km and are caused by strong magnetic fields. Sunspots are treated in more detail in Section 2.2.

2.1.2 The chromosphere

The chromosphere begins at a height of approximately 525 km, at the local temperature minimum at the upper end of the photosphere, as mentioned above. This atmospheric layer is characterised by a steady temperature increase from its lower to its upper bound, and extends to about 2100 km above $\tau_{500} = 1$. From 4 400 K to 10 000 K, the temperature increase is accompanied by a drop in gas density of a magnitude of more than 10^4. In fact, the radiated intensity of the chromosphere also drops an inverse factor of 10^{-4}, and visible wavelengths originating in the chromosphere are therefore normally drowned out by photospheric emissions. This restricts observations of the chromosphere to wavelengths especially sensitive to the chromosphere, as to avoid this effect. The chromosphere appears as a very dynamic atmospheric layer with several notable features.

On scales of about 30 000 km, supergranulation can be observed in the chromosphere, large-scale convection effects. Also notable observable features, spicules are filaments of gas pointing approximately vertically away from the sun, and have lengths of the order of 10 000 km, and lifetimes of approximately 15 min. These individual lifetimes are short, but a few percent of the sun are covered by spicules at any given time, making spicules ubiquitous. Spicules exhibit an outward mass velocity of approximately 15 km/s are therefore quite dynamic features.

2.1.3 The Corona (and the transition region)

At the outer edge of the chromosphere, at a height of approximately 2 100 km, the solar atmosphere is characterised by a sudden and dramatic increase in temperature. This region is know as the transition

region, and precedes the corona. Over the transition region, the temperature increases rapidly by over 10^5 K, at which increase slows. The increase however still culminates at over 10^6 K. The transition region is relatively small, and extends over a height of approximately 100 km, and therefore ends at a height of 2 200 km, at which point the corona begins.

The corona is characterised by the now rather steady temperature profile following the transition region. Temperature measurements for the corona are not straight forward, since it is a non-LTE gas, with very low densities. However, consistent measurements using highly ionised atoms place the temperature at above 2×10^6 K. The corona has no clear outer boundary, and extends far outward from the sun. At the inner edge of the corona, the particle density is around 10^{15} particles/m^3, whereas the density is around 10^7 particles/m^3 at the orbital distance of earth. When referring to the solar particles emanating from the corona at the extreme distance of the earth orbit, it is usually referred to as solar wind. The energy emanating from the corona is around 10^6 times less than that from the photosphere.

2.2 Sunspots

Since this thesis deals specifically with phenomena occurring in sunspots, a short review of the basic properties of sunspots is given here. Sunspots are situated in regions of strong magnetic fields and can reach sizes of up to 30 000 km, as mentioned earlier.

The strong magnetic fields in which sunspots are born inhibit efficient convection of hot material from deeper layers of the sun. This effect therefore lowers the temperature around these strong magnetic fields. The lower temperature in turn lowers the radiative output and makes sunspots appear dark compared to the surrounding solar surface.

A classical full-grown sunspot consists of a darker center called the umbra, and a slightly brighter border-region dubbed the penumbra, which may fully enclose the umbra. The penumbra has a filament structure, with strands of plasma pointing away from the umbra, tracing the magnetic field lines outwards. The magnetic field lines are modelled as vertical in the center of the umbra, tending gradually more to the horizontal as one moves outwards into the penumbra. More complex sunspots are possible, where the umbra may be crossed by so-called lightbridges. Lightbridges have higher intensity than the umbra and may somewhat resemble the penumbra.

Sunspots are usually found in groups, with a dominant sunspot leading in the direction of the solar rotation. Pores are the cousins of sunspots, but are smaller in size and lack a fully formed penumbra. Pores usually trail, or are in the vicinity of sunspots. Sunspot activity follows an 11-year cycle, tracing the polarity reversal period of the sun.

Figure 2.2 shows an example of a complex sunspot, imaged in both the Ca II wide-band and the Ca II H-line core, corresponding to the sunspot as seen in the photosphere and the chromosphere. These images were obtained at the Swedish 1-m Solar Telescope (Scharmer et al. 2003a), during an observational campaign the author participated in as part of a group from the Institute of Theoretical Astrophysics, University of Oslo.

The sunspot shown exhibits most of the properties discussed above. A fully-formed penumbra encloses the sunspot, visible in both the photosphere and the chromosphere. A lightbridge is also present, bisecting the sunspot in two roughly equal sized parts. Several pores are also visible (most clearly in the wide-band image). Some of the pores exhibit partial penumbrae, and resemble miniature sunspots. Other pores are more classical, lacking any penumbral structure.

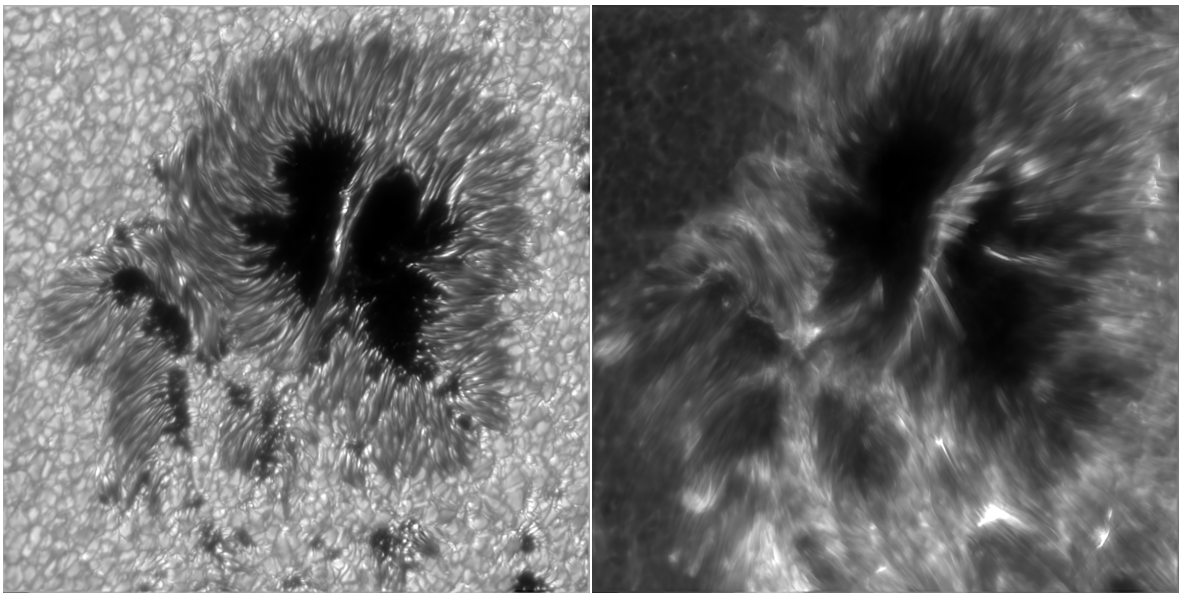

Ca-WB image Ca-H image

Figure 2.2: Example of a complex sunspot in Active Region 11785, imaged on 4 July 2013. It exhibits a full penumbra, as well as a light-bridge bisecting the umbra. There are also several pores present, both with none and partial penumbrae. The image was recorded July 4 2013 at the SST in an observing campaign the author participated in..

The images in Figure 2.2 also exemplify the general appearance of the sun in the photosphere and the chromosphere rather well. Surrounding the sunspot in the photospheric image, the pores discussed in Section 2.1.1 are clearly visible. In the chromospheric image, the filamentary structure discussed in Section 2.1.2 is also nicely exemplary.

CHAPTER 3

THE OBSERVATIONS

The observations for this thesis are obtained from the Swedish 1-m Solar Telescope (SST) situated on the Canary Island of La Palma.

First, the telescope and its setup as well as its instruments are described to some detail below. For a complete view of the entire data reduction necessary for the analysis of SST data, the reduction process of raw SST data is then described. Lastly, the specific dataset(s) obtained from the SST used for further analysis and processing in this thesis are described and presented.

3.1 The Swedish 1-m Solar Telescope

In this section, an overview of the Swedish 1-m Solar Telescope is given, highlighting its essential parts and instruments.

The Swedish 1-m Solar Telescope is an elevated optical telescope employing a partially vacuated light-path. It has a wide aperture main lens, employs adaptive optics and is setup for observing in two separate spectral ranges, blue and red, by use of a dichroic splitter. We first examine the main optical setup in the turret and tower, move on to the adaptive optics system, and then expand on the instruments in the two lightpaths after splitting.

The specific information on the SST throughout this section is obtained from Scharmer et al. (2003a), Scharmer et al. (2003b) and Scharmer et al. (2003c).

3.1.1 The Tower and Turret

The SST is a an optical telescope with its main optical setup consisting of a main 1.1 meter singlet lens with a 0.97 meter clear aperture and two 1.4 meter optical flat mirrors, with all three situated in the turret of the telescope. The main singlet lens has a focal length of 20.3 meters at a wavelength of 460 nm, and is corrected for coma, but suffers from some chromatic aberration. The SST's entry to its internal vacuum tube is the main singlet lens itself. Therefore, the lens is specifically designed for the pressure difference that it experiences, and in fact is held in place by the outside air pressure (though it has safety handles in

place in case the vacuum fails).

Following the flat mirrors is a 60 mm field-mirror and a Schupmann corrector. The corrector consists of a 305 mm lens and a 300 mm mirror, and corrects for the chromatic abberation of the main singlet lens. The lightbeam is then sent on to the adaptive optics and the optical table on which the remainder of the optical system rests. The vacuated part of the lightpath thus consists of the turret, tower and corrector assembly, terminating before the adaptive optics system.

A sketch of the main light path of the SST is given in Figure 3.1, reproduced from Scharmer et al. (2003c).

The theoretical spectral resolution of the SST is given by the size of its main aperture, the unoccluded 0.97 meter clear surface of the main singlet lens. Its diffraction limit and thus resolution is given by the Rayleigh criteria in Equation 3.1.

$$\theta_\lambda = 1.220\frac{\lambda}{D} \tag{3.1}$$

Here θ is the minimum possible resolved angle, λ the wavelength of the transmitted light, and D the aperture size. For a nominal wavelength in the midrange of the SST's capabilities of 500 nm and the aperture size of the main lens of 0.97 meters, this yields the diffraction limit given in Equation 3.2.

$$\theta_{500\,\mathrm{nm}} = 0.13'' \tag{3.2}$$

The two main central wavelengths actually observed and analysed in the present context are the Ca II 8542 Å -line and the Ca II H-line at 3968 Å. The two diffraction limits in these two lines are given in Equations 3.3 and 3.4.

$$\theta_{\text{Ca II 8542 Å}} = 0.22'' \tag{3.3}$$

$$\theta_{\text{Ca II H-line}} = 0.10'' \tag{3.4}$$

We see that observing in the Ca II 8542 Å -line entails a poorer resolution limit than for observing in the Ca II H-line, as the diffraction limit decreases with smaller wavelengths.

The turret of the SST employs an altitude-azimuth mount, and therefore rotates about two axes as it tracks the sun. Gears, motors and bearings of the turret are carefully designed to avoid vibrations of the

optical components, avoid slip-stick friction and be able to withstand the expected wind speeds at the height of the turret. Also, a high frequency for the self-resonance of the turret was required, as to make resonance with the wind unlikely. The turret is also well-sealed despite being in motion, as it must to preserve the vacuum inside the tower.

The vacuum maintained inside the telescope tower of the SST is meant to mitigate temperature fluctuations, and avoid convection of air in the large tower. Air convection inside the tower would in turn cause unstable observing conditions/seeing inside the telescope (the concept of "seeing" and its broader meaning is described in Section 3.2). A vacuum of down to 0.2 mbar is possible to achieve by continuously pumping out air, but a sufficiently low pressure of 3 mbar is achieved by a pumping of twice a day for a duration of 20 minutes. Though the large tower requires vacuating for the telescope to perform properly, it is very advantageous to cover most of the mentioned 20.3 meters focal length of the main lens before the light reaches the optical table. Also, a large tower elevates the entrance lens above the worst effects of turbulence close to the ground. These are caused by rising air heated by the ground, which itself is heated by the sun. More considerations of these effects is given in Section 3.2.

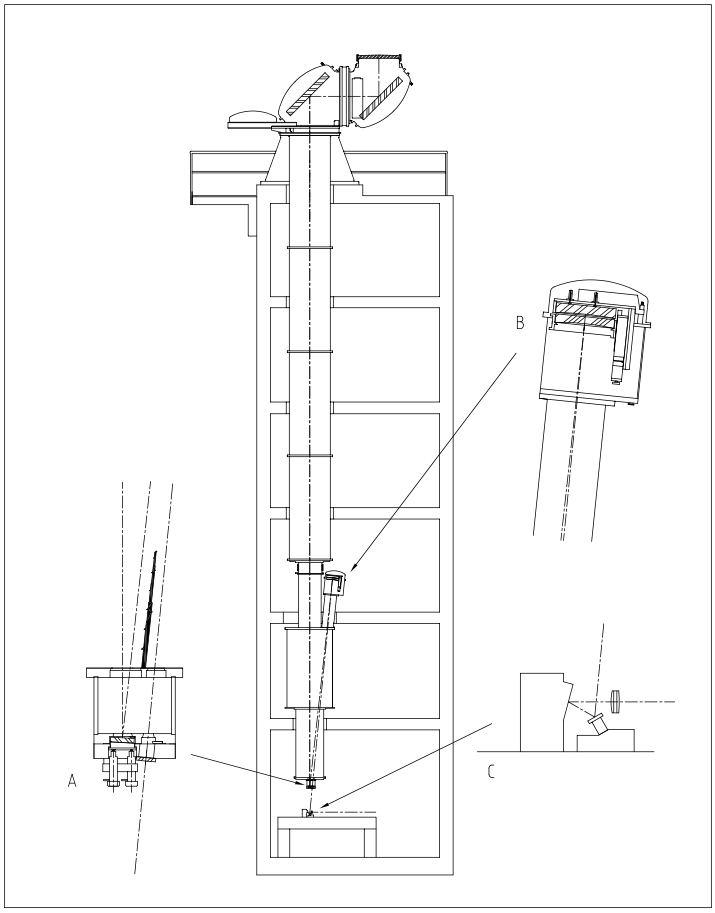

Figure 3.1: Solar Swedish Telescope, a schematic of the tower, turret and vacuum system. A: Field mirror and field lens. B: Schupmann corrector with one lens and one mirror. C: The reimaging optics, tip-tilt mirror, adaptive mirror, and re-imaging lens (optical table). Image reproduced from Scharmer et al. (2003c)

3.1.2 Adaptive Optics

The adaptive optics system at the SST is designed to counteract the effects of atmospheric distortions in the image from the tower in real time. This is achieved by modelling the incoming wavefront as if distorted by a lens in the atmosphere before reaching the main entrance lens at the turret, and subsequently trying to recreate the real image by distorting it oppositely to the lensing in the atmosphere.

In practise this is done by estimating the distortion of the incoming image, followed by actively distorting a mirror the light is passed over, cancelling out the effects of the atmosphere as much as possible. The adaptive optics system's optical components at the SST, installed after the Schupmann-corrector focus, consist of a tip-tilt mirror, a deformable mirror, and a re-imaging lens. At the time of when the observations used in this thesis were recorded, the deformable mirror was manipulated by 37 actuators. Since then, the AO system has been upgraded, and the new deformable mirror now operates with 85 actuators.

The tip-tilt mirror corrects for large-scale shifts in the incoming light beam. These could in principle also be corrected by the deformable mirror, but the maximum tilt of the tip-tilt mirror exceeds that of the deformable mirror, which is advantageous. More importantly, the tip-tilt mirror also has a faster response time, which is the main reason it is employed. Seeing varies over timespans of milliseconds, and fast response times in the AO components are therefore vital. Freeing the deformable mirror from some of the workload by letting the tip-tilt mirror handle large scale fluctuations is therefore well worth the added complexity.

Estimating the incoming wave front is made possible by using a Shack-Hartmann wavefront sensor, which consists of hexagonal elements, matching the geometry of the adaptive mirror. The sensor readings are then used to estimate the corresponding necessary deformations of the adaptive mirror. The wavefront sensor is placed in the red beam, following the dichroic splitter which is situated after the re-imaging lens. Further, a correlation tracker CCD is placed in the blue beam, which tracks sudden changes in the wavefront due to both atmospheric distortions, turret movement and drift and attempts to correct these by controlling the tip tilt mirror. Also, the correlation tracker can also correct for detected turret drift (deviation from the intended pointing) by sending corrections directly to the turret.

The components of the AO system described above are shown in the schematic of the optical table of the SST in Figure 3.2.

3.1.3 CRISP

The CRisp Imaging SpectroPolarimeter (CRISP) is an instrument used for fine sampling around specific wavelengths and is placed in the Red Beam of the SST optical setup.

The CRISP instrument was installed April 2008, and has since then provided high-quality observations. The instrument's first use is described in Scharmer et al. (2008). A full technical paper dealing with the instrument is yet to be published, and specific technical details are therefore best reviewed at SST Wiki (2013).

For the upcoming explanation of the CRISP instrument along the light beam passing through it, it is

advised to inspect the schematic of the Red Beam light path shown in Figure 3.2, reproduced from Löfdahl & Scharmer (2012).

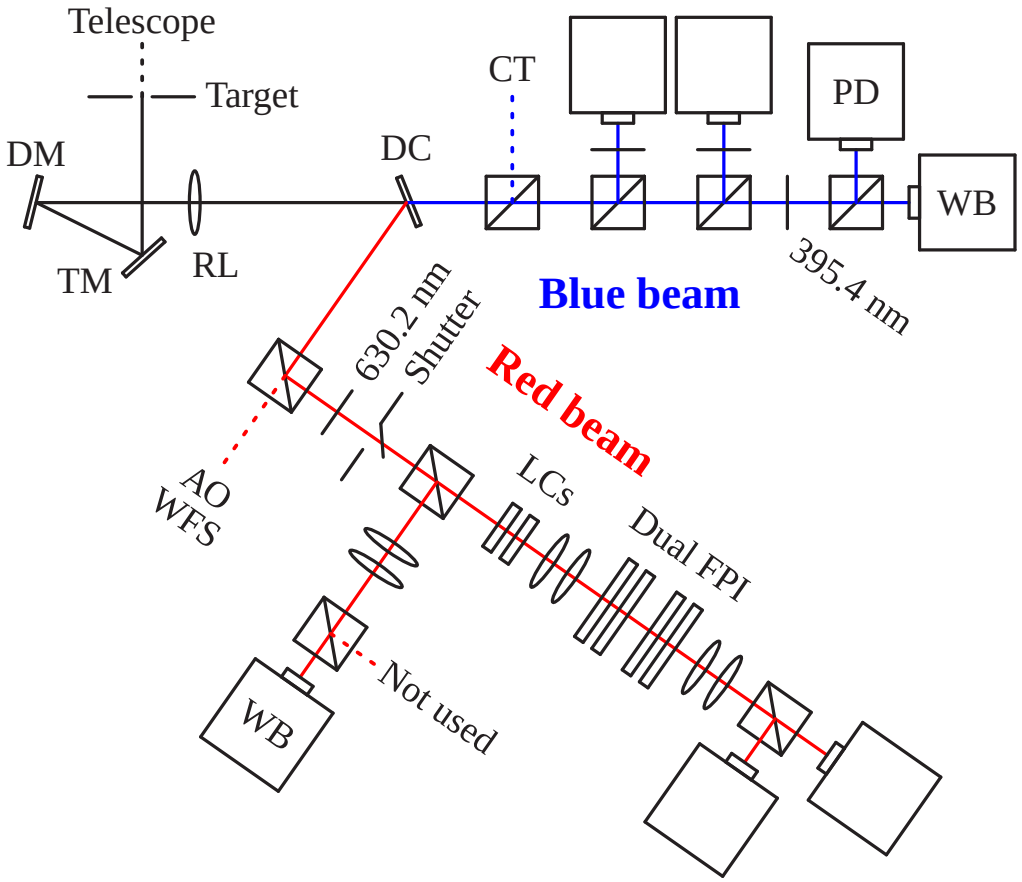

Figure 3.2: Schematic of the setup for the optical table at the SST for both the Red and Blue Beam, image reproduced from Löfdahl & Scharmer (2012). Note: the setup portrayed is not identical to the one used for the observations used in this thesis (described in Section 3.5). Specifically the 630.2 nm prefilter and shutter were instead combined in a Filter Wheel mounted with a prefilter for the Ca II 8542 Å -line (and an unused additional filter). Also, the order of the Dual FPI and the liquid crystals (LCs) was reversed. Abbreviations used: DM: Deformable Mirror, TM: Tip-tilt Mirror, RL: Re-imaging Lens, DC: dichroic splitter, WFS: WaveFont Sensor, CT: Correlation Tracker, PD: Phase Diversity cameras, WB: Wide-Band cameras.

The red beam incoming from the dichroic splitter after the AO system is first split yet again, with some of the light diverted to the Wavefront Sensor (WS), which is used to estimate the distortion in the incom-

ing wavefront and used in the AO system (see Section 3.1.2). The main light-beam then continues and is passed through an optical chopper wheel. This wheel occludes the light path at a preset frequency by rotating, and is used to synchronise the scientific cameras further down the light path. This is necessary to achieve the level of synchronicity required for later MOMFBD reduction (see Section 3.3) of the recorded data, as the CCDs' read-out times can not be sufficiently synchronised themselves. A physical synchronisation by the chopper with a properly set cadence of transmission therefore ensures equal exposure time to the CCDs before a read-out.

After passing the chopper wheel, the light beam reaches the filter wheel. The filter wheel can be mounted with several prefilters that are centered on different spectral lines. The prefilters have a FWHM of 0.30 - 0.93 nm, and can be switched during ongoing observations in as little as 250 ms for adjacent prefilters, or up to a maximum of 600 ms for opposing prefilters on the wheel, as of today. For the observations used in the present context (recorded in 2010), and the setup of the optical table as used for recording these, the switching time was a comparatively slow 1.7 s between the two filters mounted (see Section 3.5). After the filter wheel the lightbeam is split once more, with some of it diverted to a wide band camera, which records the image coming straight from the filter wheel, which is used in later MOMFBD reductions (see Section 3.3).

The main light beam then continues on to a dual Fabry-Perot Interferometer (FPI). The dual FPI is the crucial component in the ability of CRISP to scan specific spectral lines. The dual FPI consists of two tunable interference etalons, a high resolution etalon (HE) and a low resolution etalon (LE), first and second in the light path respectively. These can in conjunction be used to transmit a very narrow bandwidth of light (with the HE and LE having FWHMs of 0.0229 - 0.1073 nm and 0.1275 - 0.3483 nm in the possible passband range respectively). The dual FPI can then be tuned to transmit at given narrow-band wavelengths, thereby being able to sample a given spectral line precisely. By tuning the dual FPI between recordings, the spectral line can then be sampled at many points, and a profile of the line can be established. Tuning within a given wavelength range can be achieved in less than 50 ms.

After the FPI the light passes to an assembly of liquid crystals that can be modulated in order to measure different stokes parameters in the light beam. In the present context however, only the beam intensity, Stokes I, is used. Following the liquid crystals, the beam is split using a polarimetric beam-splitter and sent to two separate cameras. A total of three scientific cameras are therefore employed in CRISP. The cameras are three 1k×1k-pixel Sarnoff CCD cameras.

The transmission profile of CRISP in conjunction with the Ca II 8542 Å -line prefilter employed in the observations used in this thesis is shown in 3.3. The FTS Atlas sample profile of the quiet sun in this line is also shown for reference, as well as the convolved transmission profile of the prefilter and the FTS Atlas profile.

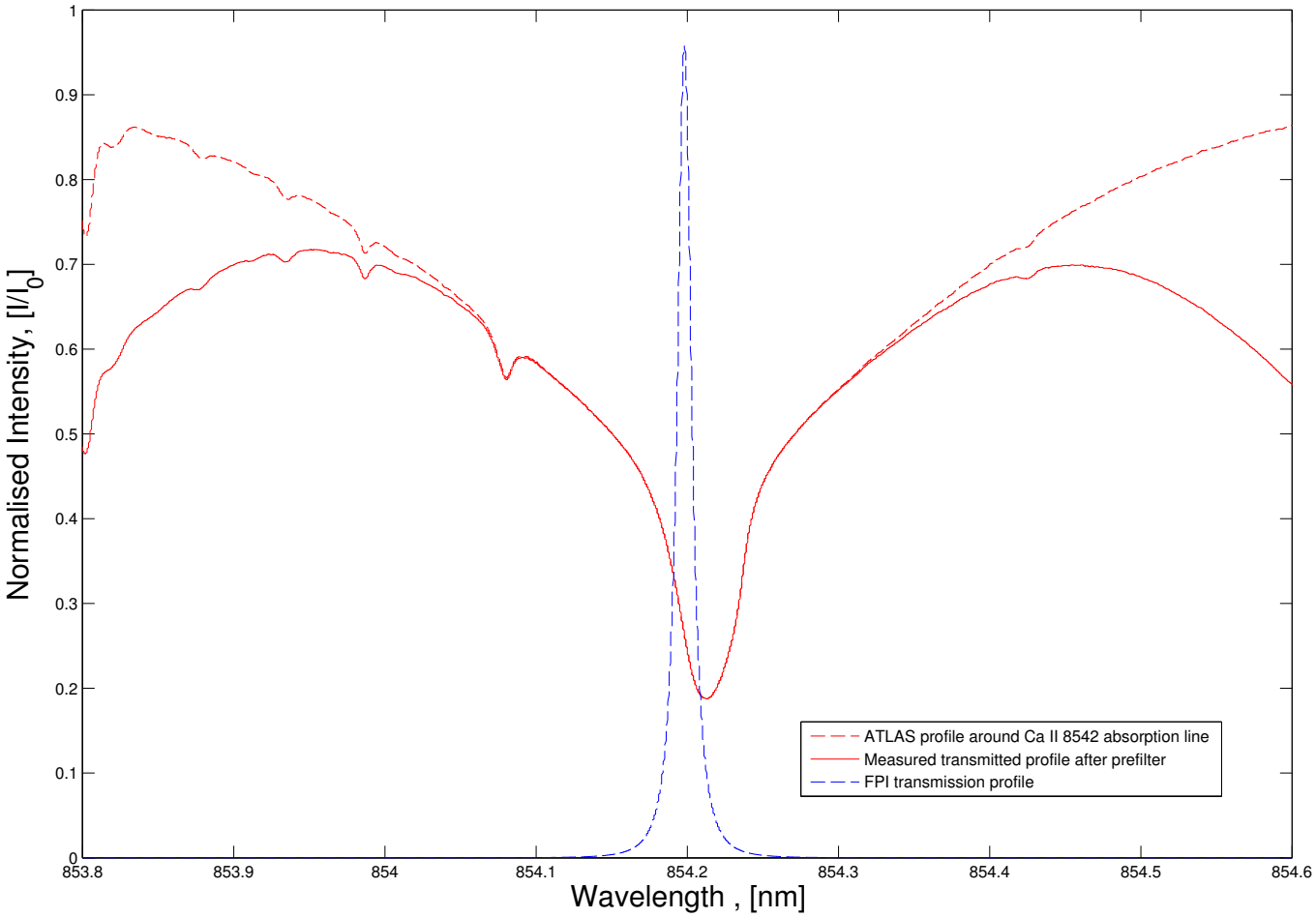

Figure 3.3: Transmission through CRISP in conjunction with the Ca II 8542 Å -line prefilter, shown together with the FTS Atlas profile of this line.

The transmission profile for the dual FPI is shown in relation to the transmission profile of the Ca II 8542 Å -line prefilter in Figure 3.4. Note the logarithmic scale, which greatly emphasises the secondary constructive interference maximums resulting from the interference in the etalons. These secondary spikes are undesirable, but are below the 1% level of the central peak, and therefore in practise the central peak is sufficiently stronger as to make them tolerable.

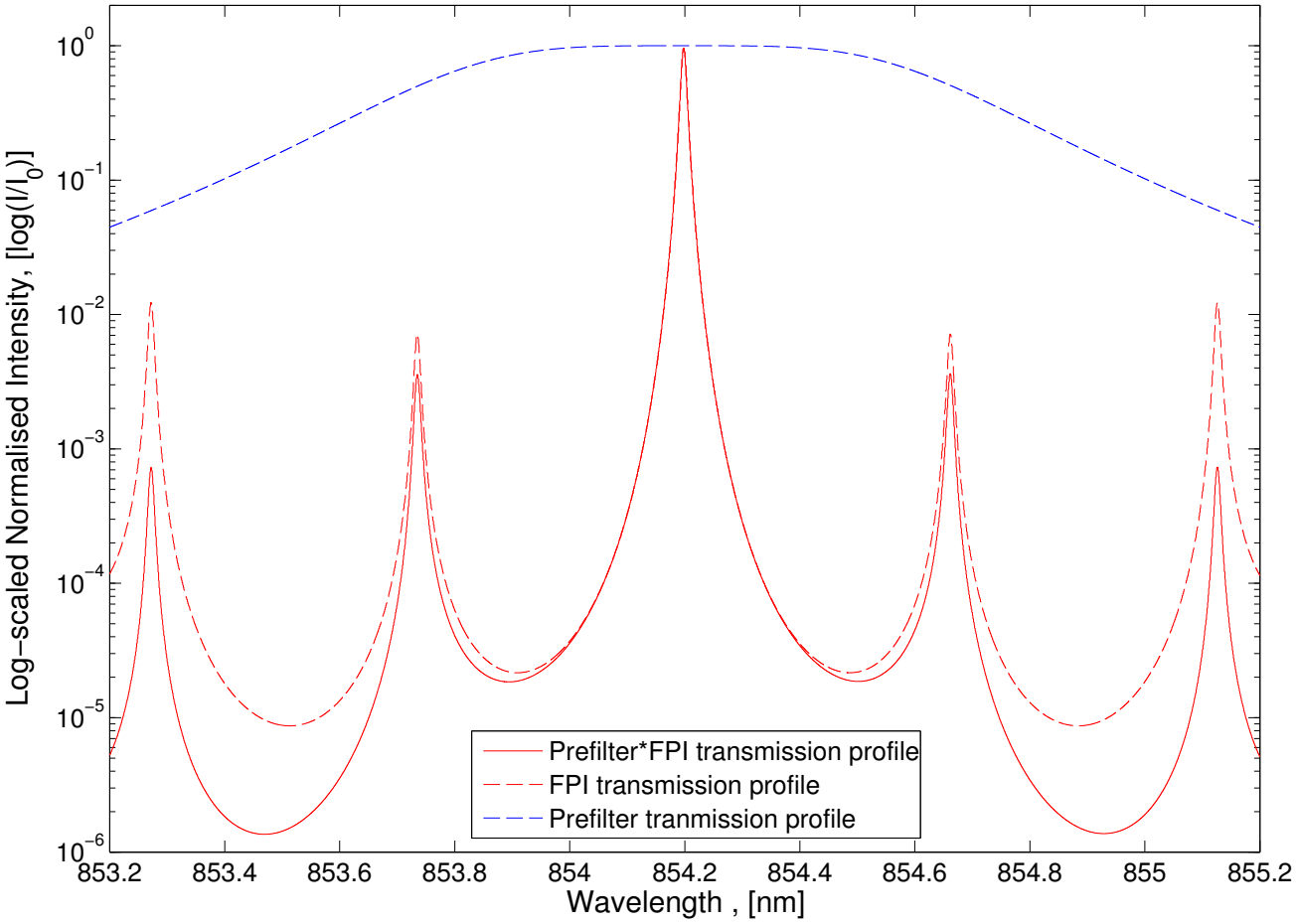

Figure 3.4: Transmission profiles of CRISP filters; Ca II 8542 Å -line prefilter and FPI.

3.1.4 Blue Beam

The other half of the main light beam after it is split by the dichroic splitter following the AO system is the Blue Beam. Following the dichroic splitter on the blue side, the first instrument is the correlation tracker, as explained in Section 3.1.2.

After the correlation tracker follows a beam splitter, splitting of some of the light beam to a camera. The main light beam after this is split yet again, diverting another branch to a second camera. A relatively wideband filter follows this second branching point which is used to sample specific spectral lines in the blue passband. This filter can also be tuned to specific wavelengths within a given line by tilting it from the standard perpendicular alignment in relation to the light beam, as described in Löfdahl et al. (2011). The tiltable filter is therefore a counterpart to CRISP's ability to probe specific spectral lines, albeit at a reduced accuracy / with a larger FWHM.

When used with no tilt, as was the case for the observations used here (see Section 3.5), the FWHM of the Ca II H-line prefilter at 396.9 nm has a nominal value of 0.11 nm (and a measured value of 0.097 nm, Löfdahl et al. (2011)). A third and final beamsplitter splits the beam off to two final cameras. The total of four cameras in the blue beam are all MegaPlus II es4020 cameras.

3.2 Comments on Seeing

Seeing is the collective term describing whether the atmospheric observing conditions for a given telescope are good or bad at a given time. These conditions are dependent on several factors, such as local and low-altitude, as well as large-scale and high-altitude characteristics of the atmosphere.

The catch-all parameter describing seeing is the Fried Parameter r_0, it has unit length, and is usually given in centimetres. This parameter is a measure of the coherence length of optical transmission in the earth atmosphere. Inversely, this corresponds to the estimated size of the isoplanar patches in the atmosphere - the scale at which the atmosphere is rather uniform. The parameter was first introduced in Fried (1966). Higher values of r_0 are preferable, as this indicates larger areas of uniform refractive properties in the atmosphere along the line of sight (LOS). At good locations, such as at the Roque de los Muchachos Observatory on La Palma where the SST is located, seeing of $r_0 \approx 20$ cm is desirable and not uncommon. This would be considered good seeing, but higher values are possible, and considered excellent seeing.

Seeing is mostly determined by temperature fluctuations in the atmosphere along the LOS towards the target (in the present context the sun). Different temperatures cause slightly different refractive properties in the atmosphere. As air-currents (wind) drag air of differing temperature across the LOS, altering the refraction, seeing worsens. High altitude winds usually cause larger-scale seeing and aberrations, whereas local temperature fluctuations, such as hot air rising from the heated ground surrounding the telescope, cause small scale disturbances, often very bad for seeing.

Thermal currents along the SST tower for example, can cause such small-scale disturbances. These are however partly mitigated by applying a heat-resistant white coating of paint to the surrounding ground and building of the SST itself. Another simple way to avoid some seeing is raising the main aperture of the telescope above ground level and the ground-based turbulences. The SST's turret sits upon its 17 meter tower partially for this reason. A taller tower would raise the turret above some residual ground-turbulence, but this was not known when the tower was built. Another effect that can cause bad seeing is simply occlusion in the LOS caused by particles in the air, an example of which is Calima. Calima occurs when dust and sand from the Sahara is blown towards the Canary Islands - sometimes to the extent of visibly reddening the sky, causing very bad seeing.

Bad seeing is of course to be avoided, and can be mitigated by factors such as site location (selecting a site with favourable seeing conditions, such as La Palma), as well as with "simple" engineering such as the application of the heat-deflecting white paint to the telescope as mentioned above. Two more modern approaches are to employ Adaptive Optics (AO) on one hand (as described in Section 3.1.2), and digital image reconstruction with which a lot of seeing can be corrected for post-facto.

The two latter approaches are vital to obtain observations suitable for modern analysis. The usage

of Adaptive Optics entails including a deformable mirror in the primary light-path of the instrument, as described in Section 3.1.2. Further, seeing can be negated to some extent using numerical methods that analyse the observations and extrapolate the effect of seeing, followed by estimating the true/ideal image of the target.

Adaptive Optics are used to remove lower-order aberrations in the image resulting from seeing, whereas numerical approaches focus on higher-order effects. The two tools reach their full potential when the instruments of the telescope, the AO system and the numerical approach are designed as a whole. The numerical method employed for SST data is Multi Frame Multi Object Blind-Deconvolution (MOMFBD). MOMFBD is briefly described below (Section 3.3), and is optimised with regard to the AO system at the SST in mind (and vice versa).

Multi Frame Multi Object Blind-Deconvolution is a method of image restoration used to mitigate the effects of image degradation due to atmospheric distortion which the AO system was unable to compensate during the observations, and is therefore a post-facto method of image restoration.

3.3 MOMFBD

The general background on MOMFBD given below is primarily based on the work laid out in van Noort et al. (2005) and van Noort et al. (2006). Further context is provided in Löfdahl et al. (2007) and van Noort & Rouppe van der Voort (2008). These sources deal with MOMFBD in the context of reduction of various SST data, and comparative analysis of MOMFBD with other methods.

In MOMFBD it is assumed that any image captured will consist of a convolution of the true image of the extended object being targeted (the solar surface) and a space invariant point spread function (PSF) as well as random noise. Here, the PSF represents the effects of seeing, eg. atmospheric turbulence/ refractive variances in the field of view, as well as the combined unaccounted image-degrading effects from the telescope. The goal is thus to isolate the most exact possible presentation of the PSF function and deconvolve the raw images using its inverse, yielding seeing-corrected images.

Motivational-wise, MOMFBD can best be summarised in reverse order of its name-giving constituent parts:

1. Blind-Deconvolution

   As mentioned, the ultimate goal is to estimate the PSF for whatever image recorded, and to deconvolve the PSF effect out of the image. However, theoretically there is an infinite amount of PSFs that could fulfil this prerequisite when one only considers a single image. The problem is thus ill-constrained, and it can be said that one begins with a blind" assumption on the PSF's form.

2. Multi Frame

   The Multi-Frame part of the process refers to capturing several frames "simultaneously", meaning with a very fast cadence for capturing a given image, over a duration of which the object is assumed to be unchanged. This places natural constraints on the cadence, with regards to the rate of change

of the sun/object. For the sun, this is commonly estimated by the sound-velocity at the given height observed. Even though the object is assumed unchanged (and for practical purposes has to be for the method to be successful), the seeing will be variable across the burst of images recorded in quick succession. This therefore yields additional information about the PSF for each given frame, since the theoretical object occluded by it is constant. To further constrain the PSF solution space, we then turn to the Multi Object component of the method.

3. Multi Object

   The Multi Object component of the method involves the recording of several images of the same FOV in different wavelengths - which produces Multiple Objects, as different wavelengths sample different heights in the solar atmosphere. This in turn means the images will portray different "objects" in the sense of different height cross-sections on the sun, that differ in structure/morphology. In the present context this translates to recording images in the wide-band filter in the red beam and images from CRISP, or alternatively recording images in the wide-band filter of the blue beam and in the Ca II H line-core filter.

   Each different object is imaged multiple times, as outlined in the Multi Frame step. Thus we now also gain the added information of having different objects recorded at the same time, as the images are recorded using a beam splitter and a chopper to record simultaneously on different cameras. Thus, for any scan, which corresponds to the eventual single time-frame of the data, we can correlate images of different objects that are affected by the same seeing effects, as well as images for each object with different seeing distorting the images.

Using the information gleaned from the Multi Frame and Multi Object steps above, the Blind-Deconvolution scheme is then employed to estimate the different PSF functions in sub-patches of each object-wavelength for each scan. These sub-patches, which overlap, correspond to the isoplanar patches over which the PSF is assumed constant, and is thus correlated with the Fried parameter r_0 and must be chosen in size accordingly. The patches are then deconvolved separately, and stitched together for each actual time frame and wavelength. Each line-scan is thus MOMFBD reduced.

The SST is setup for MOMFBD reduction, and the Multi Object step is performed using a line-scan resulting from the use of the CRISP instrument (in the present context and relevant observations, in a scan around Ca II 8542 Å -line), with each sampling position recorded several times in rapid succession.

MOMFBD is conceptually strong in the sense that it assumes little about the nature of the PSF and incoming wavefronts, and is thus well suited to high-cadence data as statistical independence between individual images is not as important as for other methods, such as Speckle Imaging (as described in Löfdahl et al. (2007), which compares MOMFBD and the Speckle Imaging method). Also, employing a phase-diversity channel, it can in some cases correct for static instrumental aberrations from the images as well. MOMFBD is however numerically expensive compared to Speckle Imaging.

3.4 Post processing of observations

After the SST observations have been MOMFBD reduced and been corrected for as much of the seeing effects as possible, some further post processing is still necessary.

The rotation of the SST's turret as it tracks the sun during observations introduces a continuous corresponding rotation in the image sequences. This rotation must be corrected for in all recorded time frames to achieve a steady FOV. The derotation of the images is performed by computing the theoretical angles of rotation in the images from the position of the sun and a pointing model for the turret. The position of the sun and pointing of the turret are of course changing throughout the timespan of the observations, and so must be computed and combined for the calculation of the derotation angle throughout the timeseries.

Following derotation of recorded observations, they must also be aligned for the case of when observations were recorded in both the Blue and the Red beam, as is the case in the present context. Different images from each of the beam halves are already internally aligned by the MOMFBD process, but observations obtained separately from the two beams are not. Alignment between the two beams is achieved by aligning the wide-band images in each beam. The wideband images from the two beams are used for the alignment as these are quite easily correlated, as the images are usually quite similar, and objects are clearly identifiable. This is due to the fact that the wide-band filters both capture the photosphere. A cross-correlation scheme is then employed to align the wide-band images in the two beams. As the internal images of the two beams are already aligned, all images across both beams are therefore also aligned by extension through the wide-band recordings.

After MOMFBD there will usually be residual stretching effects, dubbed rubber-sheet motions, over different time steps. This effect is caused by atmospheric distortions that are smaller than the assumed isoplanar patches in the MOMFBD reduction, and which therefore are not adequately corrected for. To mitigate this effect the observations are divided into small overlapping subfields and these are compared to images in the same wavelength but at the next time step. In the comparison, an offset between each subfield for the adjacent time frames is computed, and the the distortion between time frames estimated, and subsequently removed. This process was initially described in Shine et al. (1994).

After these final processing steps, the observations are ready for scientific analysis.

3.5 The Datasets of 28-June-2010

The observations used in this thesis were obtained by the SST on the 28th of June 2010, focusing on an Active Region (AR) containing a very well-behaved near circular sunspot with a fully formed penumbra. The observations discussed here were obtained by Luc Rouppe van der Voort[1] and Patrick Antolin[1]. The MOMFBD reductions and post processing of the observations presented here were also performed by Luc Rouppe van der Voort.

After reduction, the imaged field of view covers a size of 55.2×55.2 arcsec^2, equivalent to a distance of 40 700 km along each side of the cubical observational area. The observations were taken over a period of about 42 minutes. The sunspot was situated in the active AR11084 close to the limb of the sun. Table 3.1 gives the information on duration, pointing and area imaged for the SST observations used.

[1]Observations were made during an observing campaign at the SST by the Institute of Theoretical Astrophysics, University of Oslo

Table 3.1: General information for the SST observations of 28-June-2010

Sequence	9:18:22 - 10:00:15 (UT)
Duration	00:41:52[s]
Field of View	55.2×55.2 [arcec^2] = 40 700 × 40 700 [km^2]
Resolution	737 [km/arcec]
Scale in observations	0.059 [arcsec/pix]
Solar Coordinates	$(x, y) = (-710, -339)$ [arcsec]

As a reference on the relative position of the observed area on the sun, figure 3.5 shows an image of the full-disk sun imaged through a 450 nm filter displaying the sun's photosphere, obtained by NASA's Solar Dynamics Observatory (SDO) (Lemen et al. 2012). The image is taken on the same date as the observations from the SST towards the end of the timeseries, at 10:00:08 UT. AR 11084 is labelled, and is the only notable visible feature at the given time at this wavelength, with a very calm disk otherwise.

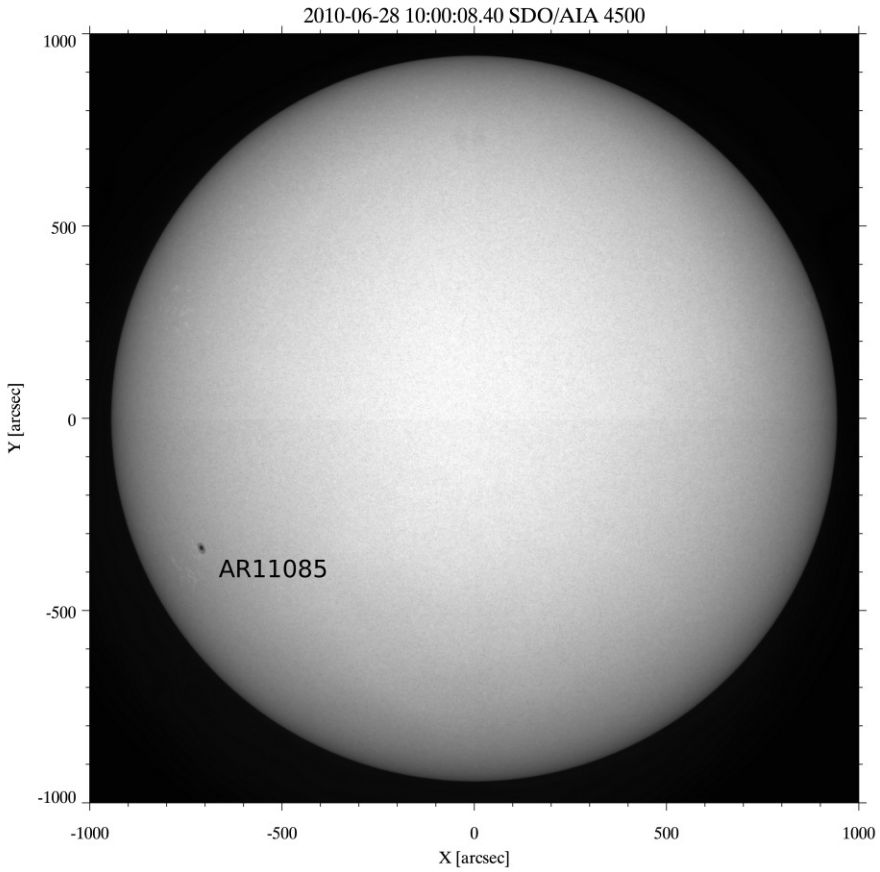

Figure 3.5: Image of the full-disk sun imaged through a 450 nm filter displaying the sun's photosphere, obtained by NASA's Solar Dynamics Observatory (SDO) (Lemen et al. 2012), Active Region 11085 is indicated.

Two sets of observations obtained during the same timespan and using the same pointing as given in Table 3.1 are used in this thesis. Both these sets of observations image the sun in passbands around spectral lines of the twice-ionised Calcium atom (Ca II). For the primary observations, CRISP (see Section 3.1.3) was used to finely sample the Ca II 8542 Å -line at 37 different positions, providing a well resolved look at this spectral line. The secondary observations were recorded from the Blue-Beam of the SST (see Section 3.1.4) using a relatively wide-band filter, centered around the Ca H-line at 3968 Å. The filter used for these observations is a narrowband interference filter, providing the option of wavelength tuning by tip-tilting. For the present observations, the tuning was however held constant to the line core of the Ca II H-line. A separate single wavelength recording around the FeI 6302 Å line was also performed during the

recording of these two sets of observations, but this recording is not used here.

For reference, figure 3.6 depicts the different atomic transitions in the Ca II atom, with the transitions marked by their associated wavelengths, with the two mentioned lines included.

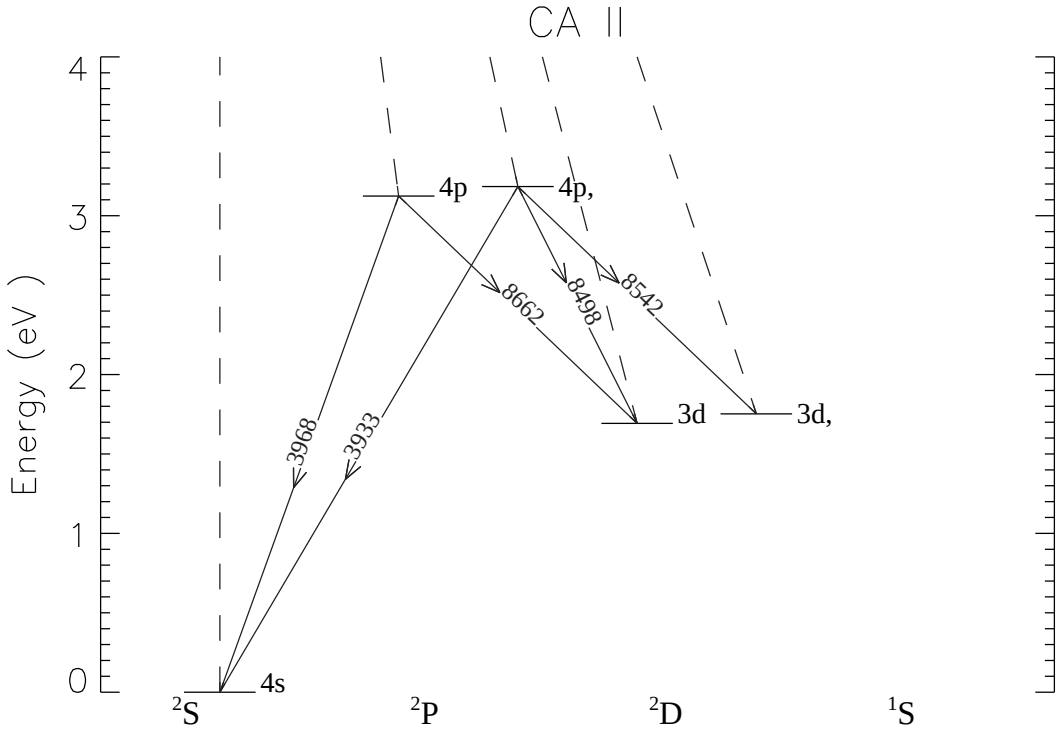

Figure 3.6: Diagram of the atomic energy transitions in the twice ionised Calcium atom, Ca II. Horizontal lines: energy levels, solid lines: bound-bound transitions, dashed lines: bound-free transitions. Reproduced from Carlsson & Leenaarts (2012).

The observations centered around the Ca II 8542 Å -line are as mentioned the primary observations used in this thesis, and the observations most extensively analysed. Table 3.2 summarises the technical information of these observations.

Table 3.2: Technical information on the primary dataset of 28-June-2010

Instrument	CRISP
Observed rate	35 [frames/s]
Calibrated line core center wavelength of prefilter	8541.6 Å
FWHM of prefilter	9.3 Å
The 37 sample position offsets around line center (See Figure 3.7)	±(0, 55, 110, 165, 220, 275, 330, 385, 440, 495, 550, 605, 660, 715, 770, 825, 880, 948, 1034) [mÅ]
Number of scans	202
Average time per scan (8542 Å)	8.55 [s]
Cadence of series	12.44 [s]

For a better understanding of the sampling of the Ca II 8542 Å -line, Figure 3.7 displays the FTS Atlas' profile of the Ca II 8542 Å -line for the quiet sun, with the sampling points of the primary dataset indicated.

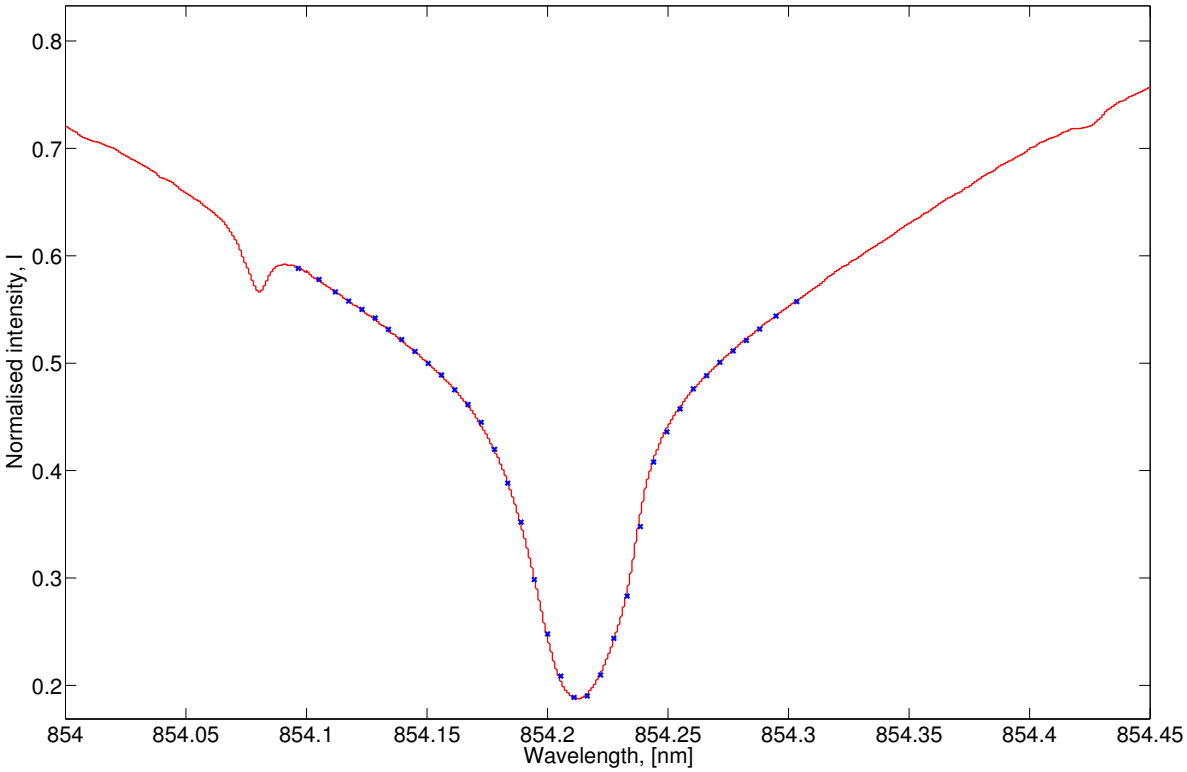

Figure 3.7: Average FTS Atlas profile of the Ca II 8542 Å -line for the quiet sun, with the sampling points in the primary dataset marked.

Example images of the entire reduced FOV of the primary dataset are given in Figure 3.8.

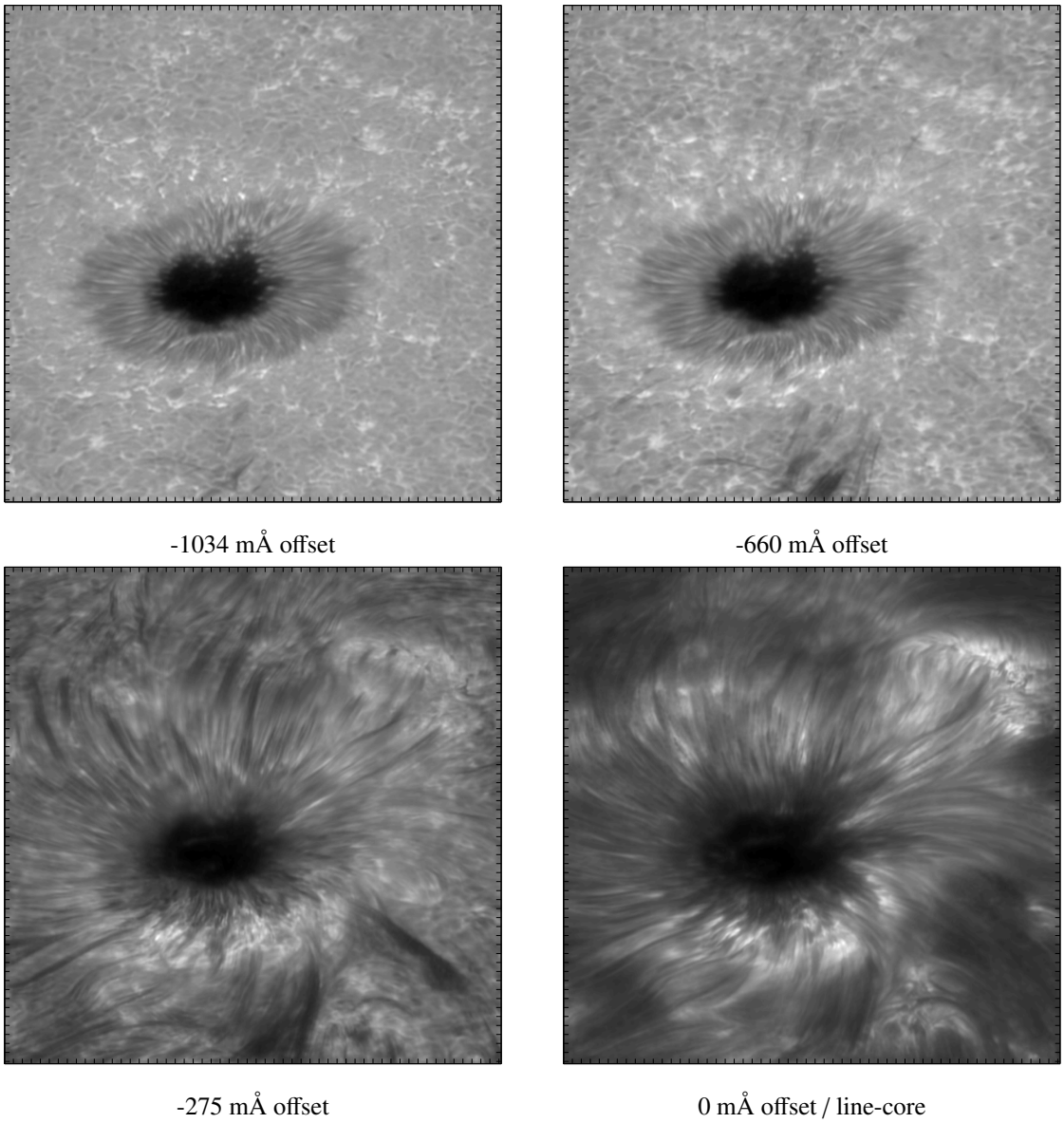

Figure 3.8: Example of different sample points in the Ca II 8542 Å -line for a single time frame in the primary observations. Tick-mark separation is 1".

The characteristics of the secondary data set used which samples the Ca H-line using a broad-band filter are reviewable in Table 3.3.

As mentioned in the table's footnote, this data set actually has a different cadence than the primary

Table 3.3: Technical information on the secondary data set of 28-June-2010

Instrument	Blue-beam cameras
Sequence	09:18:29 - 10:00:12 [s]
Duration	00:41:42[s]
Observed rate	10.83 [frames/s]
Filter	3968 Å (single spectral position)
Central Wavelength	3968.8 Å
FWHM	1.1 Å
Number of scans	404
Cadence of series	6.2⋆ [s]

⋆The cadence is an artificial result of reducing higher-cadence data to half of the cadence of the primary data set.

observations, resulting from the use of different instruments. The given cadence is that of the reduced data, which for convenience was set to half that of the primary dataset, though the actual observations had a slower recorded cadence.

An example image at a single time frame from these observations in the Ca II H-line is given in Figure 3.9.

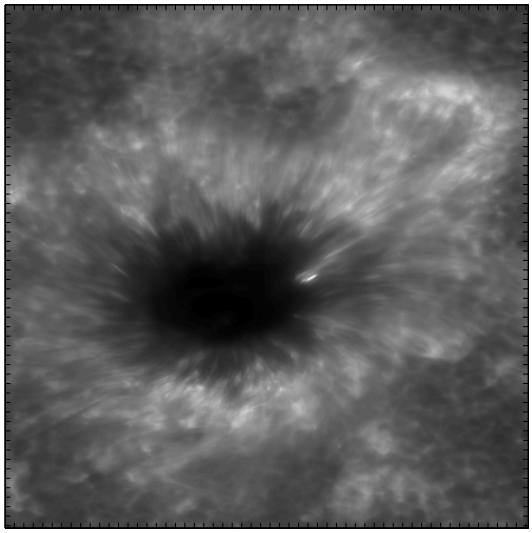

Figure 3.9: Example image from the secondary observations in the Ca II H-line, at a single time frame (note the very bright PMJ event on the right side of the umbra). Tick-mark separation is 1".

The secondary data set is used as a supplement to compare observations in Ca II 8542 Å to those in the H-line in context of the present work, but its most important utility is to justify observations in the

Ca II 8542 Å -line at all, linking the detection of PMJs in the present context to earlier work. This is possible as earlier work on PMJs has involved imaging of PMJs in the Ca II H-line (Katsukawa et al. (2007), Jurčák & Katsukawa (2008)), this is expanded upon in Section 4.2.

Also, investigating the characteristics of objects present in both lines is attempted in order to speculate on the spatial and physical properties PMJs using the properties of these lines, such as formation height and temperature dependence, which falls under Chapter 6.

CHAPTER 4

PENUMBRAL MICROJETS

Literature on Penumbral Microjets is limited, and observational papers more so. In fact, as to date, the only source of observational data on PMJs is limited to Katsukawa et al. (2007) and Jurčák & Katsukawa (2008). This will be a succinct summary of Penumbral Microjet properties as they are described in the scientific literature so far. Following this, areas of interest for further study, as well as results that may be desirable for re-examination are pointed out.

4.1 Penumbral Microjets in the literature

As mentioned previously, the only observational data on Penumbra Microjets is found in Katsukawa et al. (2007), and its follow-up paper Jurčák & Katsukawa (2008). This subsection is consequently a summary of observational results solely from these two sources if not stated otherwise.

The observations of PMJs published were recorded with the Ca II H and G-Band filters on the Solar Optical telescope on the Hinode Satellite (Tsuneta et al. (2008)). The Ca II H observations having been presented in Katsukawa et al. (2007), and further analysis employing both wavelength regions presented in Jurčák & Katsukawa (2008). The actual PMJ events were only detected in the Ca II H observations, and the G-band observations were used for supplementary inferences about their geometry.

The Ca II H filter of the SOT used in the observations is centered at 396.9 [nm] and has a bandwidth of 0.3 [nm], whilst the G-Band filter of the SOT is centered at 430.5 [nm] with a bandwidth of 0.8 [nm] (Jurčák & Katsukawa (2008)).

The data set used in both papers was recorded on 10-November-2006, with the observations directed at the active region AR10923, covering part of a sunspot.

Figure 4.1 is reproduced from Jurčák & Katsukawa (2008) and shows a sample of PMJ detections made in the Ca II H-line using the SOT onboard the Hinode spacecraft.

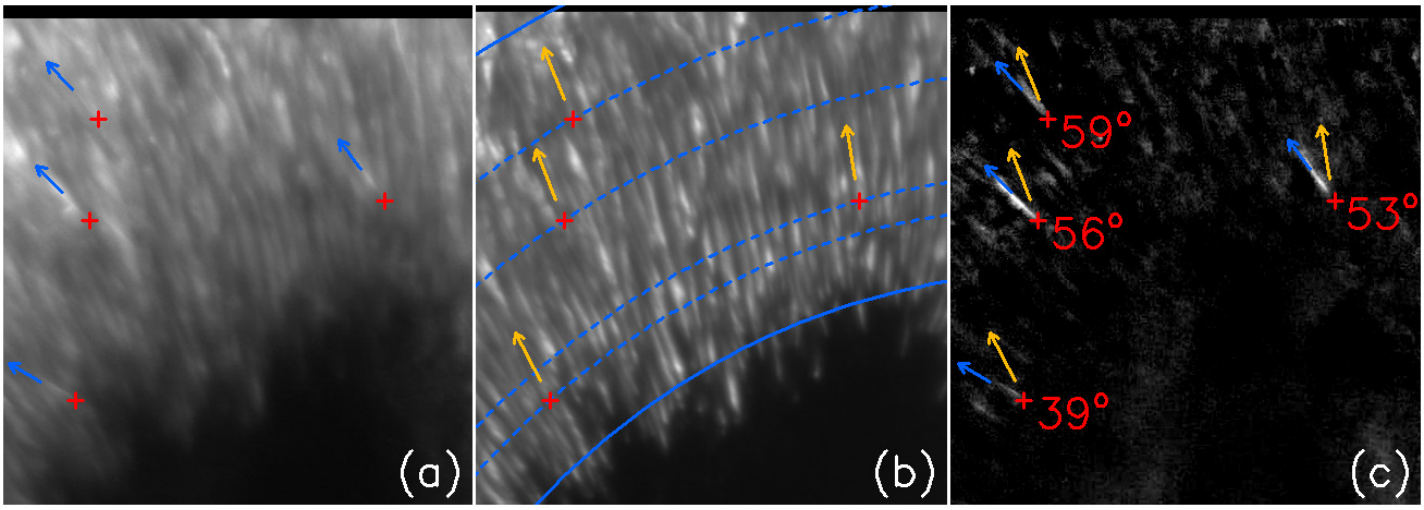

Figure 4.1: Reproduced example detections of PMJs from Jurčák & Katsukawa (2008), which employed observations from the SOT. a) Ca II H-line, b) G-Band, c) Ca II H running difference. Red-crosses mark onsets of PMJs, blue arrows their orientations, orange arrows mark orientations of fibrils. Offsets between PMJs and fibril directions are indicated in c).

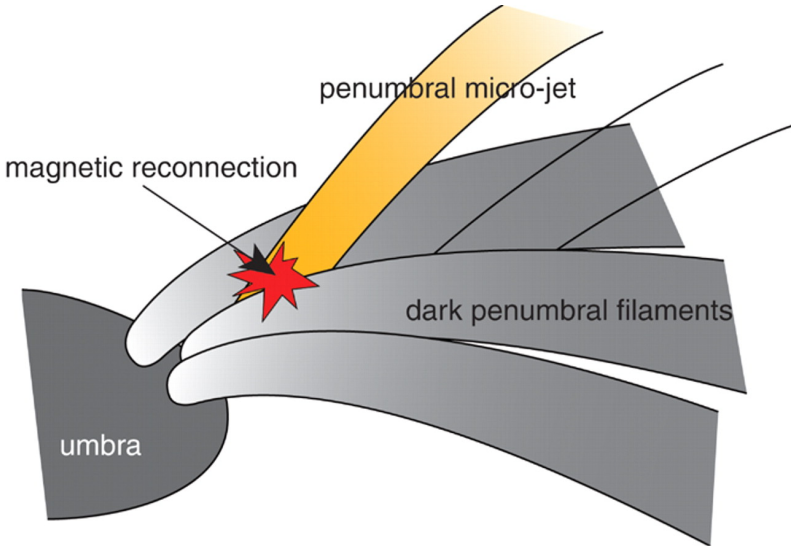

Figure 4.2: Sketch of microjet geometry, reproduced from Katsukawa et al. (2007).

Employing running-difference images in Ca II H as an aid for detection, Penumbral Microjets were manually selected and their sizes and lifetimes noted in Katsukawa et al. (2007). Furthermore, using the slopes in space-time plots the apparent rise-velocities were estimated. Also, the geometric configuration of PMJs in the surrounding solar atmosphere was inferred, as can be reviewed in Figure 4.2. Lastly, the energetics of the PMJ events were estimated from well-established atmospheric values of the penumbra.

In the second paper, Jurčák & Katsukawa (2008), an analysis of PMJ inclinations with respect to the solar surface was carried out employing G-Band observations that were co-observed with the Ca II H observations previously used.

This was achieved by tracing the PMJs directions in Ca II H images, and tracing the local fibril direction in G-band images for each PMJ. The apparent angle between these two directions, combined with the heliocentric angle and the symmetry line connecting the microjet onset position and disk center, the calculation of the inclination was carried out following the approach from Müller et al. (2002). The formula for the inclination used is given in Equation 4.1.

$$\phi = \arctan\left(\frac{\sin\gamma' \sin\phi'}{\cos\gamma' \sin\theta + \sin\gamma' \cos\phi' \cos\theta}\right) \tag{4.1}$$

Here θ is the heliocentric angle, ϕ the azimuth angle in the line-of-sight frame, ϕ' and γ' are the azimuth and inclination respectively, with respect to the local reference frame, characterised by the z axis (local normal line), and the x axis (symmetry line). A schematic of the two coordinates systems is reproduced from Müller et al. (2002) is given in Figure 4.3.

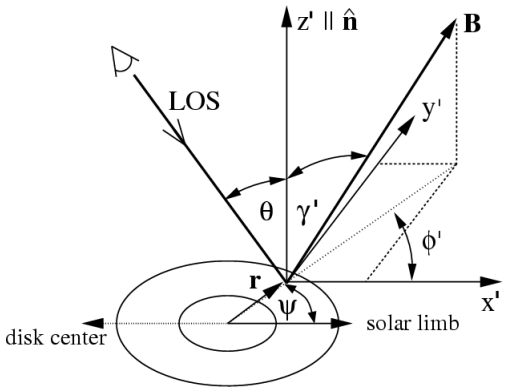

Figure 4.3: Schematic of coordinate systems and how they relate - Line Of Sight frame and Local Reference Frame, as shown. Reproduced from Müller et al. (2002).

The inclinations of PMJs is then correlated with their positions within the penumbra. Here, a positive correlation is reported, connecting the inclination angle with the radial distance outwards from the sunspot center.

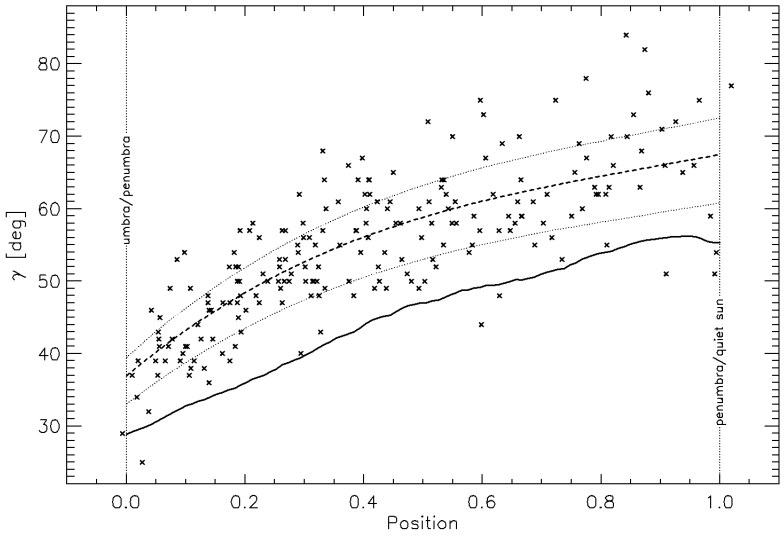

Figure 4.4: Inclinations of Penumbral Microjets inferred from Ca II H and G-band observations from SOT observations, reproduced from Jurčák & Katsukawa (2008).

Using the measured lengths and widths of detected PMJs, an estimation of the thermal energy in a PMJ event was estimated in Katsukawa et al. (2007). The thermal energy was estimated as given in 4.2.

$$E = \frac{3}{2} n k_b T V \tag{4.2}$$

Here, E is the thermal energy, n the number density in the atmosphere, k_b is the Boltzmann constant, T the temperature, and V the volume of the event. For assumed values of $T = 10^4$ K, $V = 2000$ km $\times(300\text{km})^2$ and $n = 10^{18}\text{m}^{-3}$, the reported value for the energy was the one given in Equation 4.3.

$$E = 2 \times 10^{16}\text{J} \qquad \text{or} \qquad E = 2 \times 10^{23}\text{erg} \tag{4.3}$$

Table 4.1 summarises all the inferred morphology and dynamics of PMJs as found in the mentioned papers except for the investigated inclinations of PMJs, which are reproduced in Figure 4.4.

Table 4.1: Summary of Penumbral Microjet morphology and dynamics from the literature

Length	(1000-4000)* [km]
Width	300-400 [km]
Lifetime	1 [min] or less
Apparent rise velocity	50-100 [km/s]
Estimated Energy	2×10^{16} J

* Some PMJs were reported to have lengths of up to 10 000 km.

4.2 Notes on observing PMJs in Ca II 8542 Å

Before a proper investigation of PMJs in the Ca II 8542 Å observations from the SST (see Section 3.5) can be begun, a justification of what is in fact going to be investigated is in order. PMJs have to date only been detected in the wide-band filter of the Ca II H-line of the SOT onboard the Hinode satellite. This means that before an analysis of PMJs in the Ca II 8542 Å -line can be performed, a case has to be made that what is investigated is in fact the same type of object as those reported in Katsukawa et al. (2007) and Jurčák & Katsukawa (2008).

The means to do this lie in the secondary Ca II H-line observations recorded simultaneously with the primary observations in the Ca II 8542 Å -line (see Section 3.5). As the secondary observations are in the same wavelength range as those obtained from the SOT's Ca II H-filter reported on in Katsukawa et al. (2007) and Jurčák & Katsukawa (2008), it can be expected that PMJs are detectable in the Ca II H-line observations from the SST. Furthermore, if PMJs are readily detected in the secondary observations and an apparent connection to features in the primary observations can be made, one may safely assume that these are the PMJs as reported on, visible in both wavelength ranges.

To investigate if PMJs are present in the secondary observations, they were manually analysed using the software CRISPEX (Vissers & Rouppe van der Voort 2012), and features fitting the description of PMJs (short lifetimes, jet-like, small-scale) were noted. A selection of found features fitting with observed PMJ properties are shown for two time frames in Figures 4.6 and 4.8. These objects are very similar to those reported on in Katsukawa et al. (2007) and Jurčák & Katsukawa (2008), and it is safe to conclude that they are the same type of object.

Following this, it was attempted to tie observations of these PMJs to similar features in the Ca II 8542 Å observations. It was quickly discovered that features with very similar properties were easiest identified in the blue wing of the Ca II 8542 Å -line, specifically at an offset of -275 mÅ from calibrated line center at 8541.6 Å. Consequently, clear instances of features appearing in both the Ca II H-line observations and the Ca II 8542 Å observations were identified. Observations of PMJs present in both these wavelengths are given in the pairs of Figures 4.5 and 4.6, and Figures 4.7 and 4.8. In the figures PMJs that were identified by eye in both sets of observations are marked by arrows at the same pixel positions for clarity.

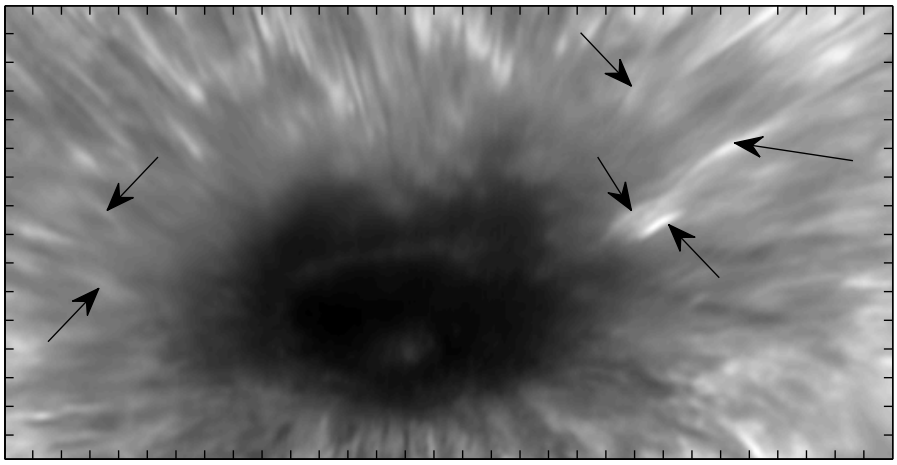

Figure 4.5: Frame number 187 from primary observations, at offset of −275 mÅ from calibrated line center at 8541.6 Å. Penumbral Microjets observed by eye are marked with arrows. Tick-mark separation is 1”

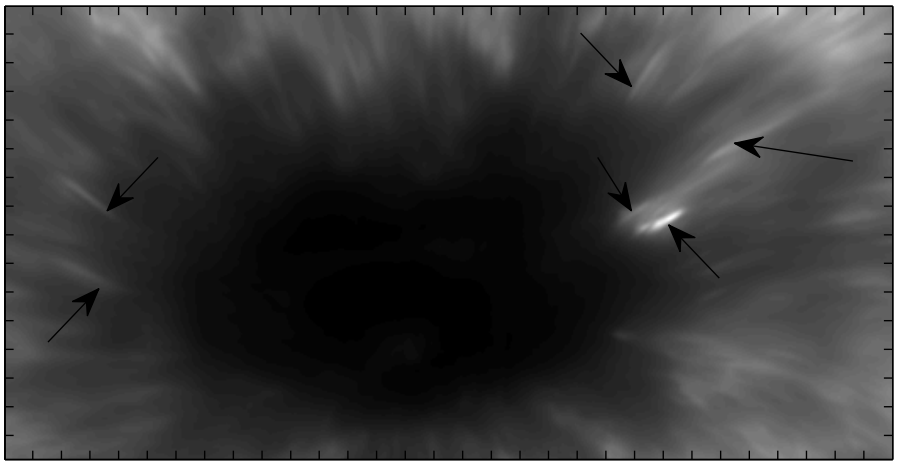

Figure 4.6: Frame number 187 from secondary observations, at calibrated line center 3968.8 Å. Penumbral Microjets observed by eye are marked with arrows. Tick-mark separation is 1”

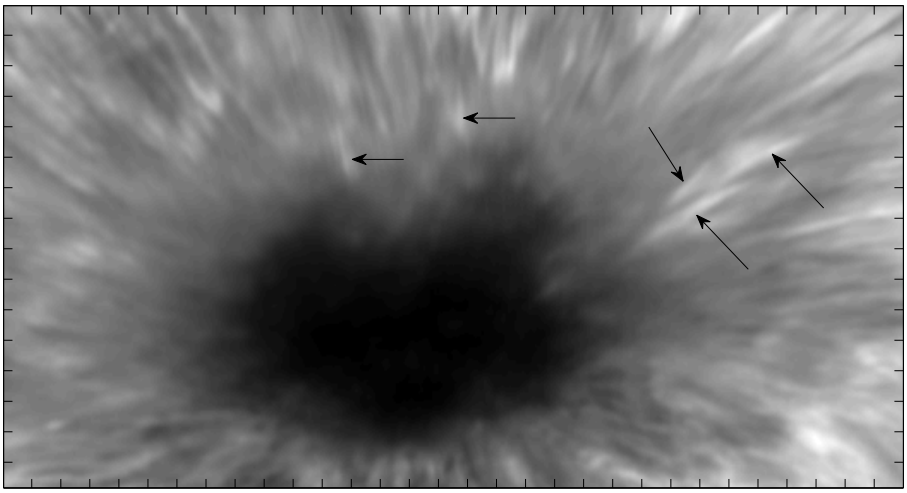

Figure 4.7: Frame number 122 from primary observations, at offset of −275 mÅ from calibrated line center at 8541.6 Å. Penumbral Microjets observed by eye are marked with arrows. Tick-mark separation is 1”

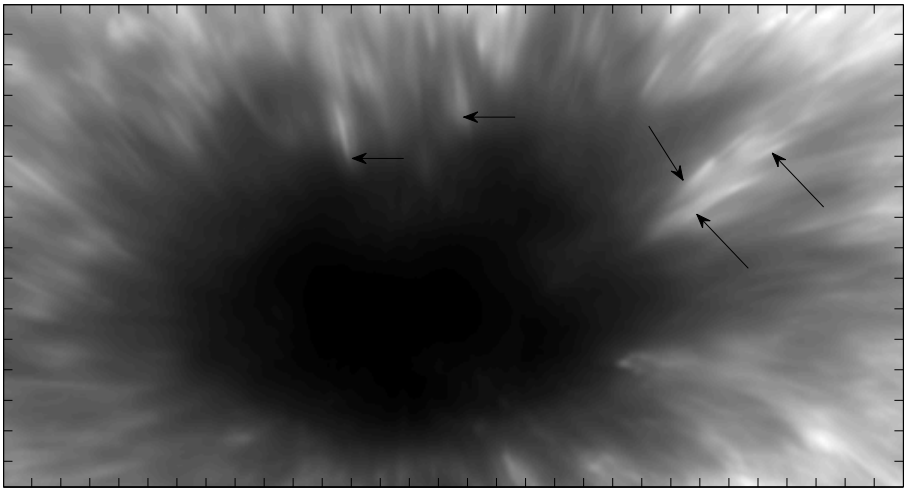

Figure 4.8: Frame number 122 from secondary observations, at calibrated line center 3968.8 Å. Penumbral Microjets observed by eye are marked with arrows. Tick-mark separation is 1”

4.3 Motivations and areas of interest

Reproduce/ Refine: Microjet lifetimes, morphology, dynamics and inclinations.

New results: Spectral signatures, maybe infer more formation from this, doppler shift.

CHAPTER 5

METHODS

5.1 Pipeline Overview

The analysis presented and carried out during the course of this thesis following the selection of the SST-reduced observational data (covered in Section 3.5) can be summarised as the steps below. These steps concern the primary dataset detailed in Section 3.5 unless otherwise mentioned.

1. *Normalising the spectral lines*

   Normalisation of individual spectral data points in the observations. Each data point consisting of the 37 intensities sampled around the line-core is summed, and each sampled intensity is divided by the result. This is necessary to alleviate the intensity variation in distinct spectral signatures due to effects such as the intensity variation from solar disk-center to solar limb and local variations in brightness. The resulting normalised data set is then used in further analysis. See Section 5.2.

2. *Principal Component Analysis*

   Further reduction of pre-reduced (and normalised) SST observational data in preparation of object recognition. The PCA of the data reduces the size of the data set, both in memory and dimensionally, reducing computational workload, and preventing high-dimensional analysis problems in later analysis of the data. See Section 5.3.

3. Object classification using the *k-Nearest Neighbour algorithm*

   Detection of PMJs using the PCA reduced normalised observational data. The k-NN algorithm produces raw classifications of all pixel-positions and time frames, producing binary images signifying the detection of PMJ like spectral objects and non-PMJ areas. See Section 5.4.

4. *PMJ primary statistics extraction*

Processing of raw classifications into labelled objects followed by object -verification, -tracking, -statistical analysis and accompanying parameter extractions. The processing cleans the raw classifications, first rendering them useful for analysis, extracting coherent objects in time and space. Following this, a collection of statistical information on these objects is possible. Thirdly, further second degree analysis of both the primary statistical data (statistics in relation to other features of the observations, such as the image background) can be obtained. See Section 5.5.

5. *Final analysis/results*

Further analysis of the found object statistics and derivation of secondary characteristics of PMJs. All information is gathered and analysed in an overall description of the collected objects in an effort to yield a coherent statistical view PMJs. This is followed by derivations of physical descriptors of PMJs in general. See Section 6.

Each of the steps above will be expanded upon and described in detail in the following sections. The motivation behind the different methods or steps will be outlined, as well as the reasoning behind their suitability for the problems at hand. Furthermore, the relevant theoretical background will be presented, and the numerical implementations where applicable commented upon.

5.2 Normalisation of the data set

For any observations of the sun that cover a large field of view, the gradual systematic intensity variation due to limb-darkening will be apparent. Furthermore, local (random) intensity variations will inevitably also be present. Both of these variations can be problematic in the context of object recognition using these observations.

For any detection scheme, manual or automatic, some sort of selection criteria, measurement of similarity, or other means of comparison is used to classify objects of interest. For manual detections, this usual means a combination of morphology and relative intensity to the background using pre-existing knowledge of the phenomenon. For automatic detections, as has been mentioned, relative intensities (usually in only one or few spectral positions) to the background is a common criteria. In the first instance, no correction for limb darkening is usually needed, as the relative intensity of objects is apparent in by-eye detections. In the second case, a correction is often necessary, and the image can be corrected for limb darkening using either an extracted value of average intensity variation along the limb-to-disk-center line, or using a theoretically derived limb darkening intensity function. Random intensity variations in the data are an inherent property of the sun (assuming the observations are not effected by additional introduced noise), and are therefore in a sense 'uncorrectable'. Furthermore, these random variations due to differing temperatures, densities, etc. will in fact be properties reflected in the objects' own variations, and so not something that should be corrected.

The approach chosen in the present detection scheme is however unique in that it focuses on the relative similarity in the *spectral* signature of objects as a means of classification (though that signature will be further analysed and condensed before actual detections are performed). This implies that the actual metric of similarity in this case is the *shape* of the spectral signature of objects and non-objects. This is opposed to using the relative intensity of objects compared to the immediate (or wider) background in a single or only few wavelengths as an identifier. In theory, relative intensity differences in one or a

few sampled wavelengths used as a detection criteria is an extremely low- resolution spectral signature comparison. However, when performing a comparison in high spectral resolution, as is the case in this work, the signature itself can be normalised to an individual metric for each data point. This ensures that intensity variations in the different samples of intensity will be negated to a large extent, assuming the variation is mostly uniform across the sampled spectral region (across the 37 wavelength sample-points).

Thus, normalising the data points will effectively negate the intensity variation due to limb darkening in the data set. Furthermore, even though intensity variations in different wavelengths may be a distinctive property of the object under study, and of interest in later analysis, normalising will reduce these to some extent, and ease detection further.

The simple normalisation of the individual spectral lines in the primary data set is detailed for clarity in Equation 5.1. Here I_{s_i} is the intensity at sampling position s_i, I_{line} is the original intensity vector of the line, and $I_{norm.line}$ is the normalised intensity vector.

$$I_{line} = (I_1, I_2, \ldots, I_{37}) \tag{5.1}$$

$$I_{norm.line} = \frac{I_{line}}{\sum_{i=1}^{37} (I_i)} \tag{5.2}$$

Computationally, this operation is readily achieved by a simple pass through the data set. During the pass, all detections are summed and normalised, and a new normalised data set is saved. This data set is then used in further analysis, processing and eventual detection of objects.

The theoretical motivation behind the normalisation is outlined above, but its effectiveness was none the less discovered in practise. The straight forward approach of using the original reduced data set from the SST without normalising the intensity vectors for detections (using the k-NN algorithm both in conjunction with PCA and without) yielded such poor results in initial testing as to near uselessness. Introducing the normalisation with the argument that the actual signal in the intensity vectors sought was the shape of the object signatures, detection accuracy improved dramatically. Again this highlights the immense value of high spectral resolution observations, and that solar phenomena are complex objects which are best understood not only in terms of morphology, dynamics and lifetimes but also as objects across wavelength. Visually, normalising the intensity vectors means bringing them to a similar relative intensity in the different intensity sampling points provided that the shape of the spectral signatures are similar.

The present detection scheme highlights in its approach the 'spectral morphology' of an object as a powerful descriptor. This descriptor may enable detections that would not be made by other detection schemes, as they may neglect a very distinct property of an object. Spectral signatures were used as identifiers and as a means of detection before high resolutions telescopes were ever available, and many phenomena were first discovered and named using spectral signatures captured on photographic plates. With the advent of high spatial resolution telescopes, detections by image analysis have become more common, and thus spectral features may have lost their prominent status as a means of classification. In the present work, somewhat of a return to detection by spectral analysis is made, at the same time as image analysis is extensively used for verification and further analysis, in an amalgamation of both approaches.

5.3 Principal Component Analysis

In this section Principle Component Analysis is introduced in the context of this thesis. First, its workings are roughly outlined and motivations given for its use. Then, the mathematical and numerical underpinning and their implementation are presented and explained. Following this, the practical application of the method on the observations in the Ca II 8542 Å -line presented in Section 3.5 is explained, and its results are presented.

5.3.1 PCA: Introduction and Motivation

Principle Component Analysis (PCA) is a potent tool for the analysis and reduction of high-dimensional data. Using PCA a multidimensional data set with inter-correlated variables is transformed into a set of linearly independent uncorrelated variables with an accompanying basis.

Each variable/Eigenvector in the new basis will have an associated amount of variance, and the new basis variables are ordered from highest-to-lowest associated variance. As each variable has a specific amount of variance that it contributes to the data set, one can then calculate how much a subset of these variables accounts for of the total variance in the data set.

This means that one can neglect variables that are deemed unimportant (they contribute less than a certain percentage to the total variance) and select a subset of variables that describes the original data set sufficiently well. The variables in this subset are then commonly called the Principle Components of the data set. Both the full new basis and the Principle Component basis can then be analysed. The full new linearly independent basis is equivalent to the original data set, and expressing the data set in this basis yields an informationally equivalent data set, albeit along new Eigenvectors. Expressing the data set using the Principle Components will reduce the information-content of the data set, but by a known amount.

PCA has several benefits. One feature is the quantification of the amount of variance associated with different variables of the data set, which in most cases can be equated with the associated informational content. Furthermore, the low-variance components of the data set can often to a certain extent be equated with noise, and the procedure can therefore function as a noise reduction method. As the data set expressed in the Principle Component basis can be linearly-transformed back to the old number of dimensions, this means that one can compress the data set to a lower number of dimensions - thereby reducing its size. The new data set can also be decompressed back to its original basis, albeit with an associated informational loss. This loss is however strictly defined. As alluded, this can also be viewed as a reduction in normal distributed noise, since the low-variance variables may be equated to low-variance noise. Additionally, many data analysis methods in which different multi-dimensional data points are compared in some fashion, will experience performance loss when there are excessively many dimensions in the data. This means that PCA is very aptly suited to reduce the number of dimensions before further analysis of the data, while retaining the important informational content of the dataset.

Thus, for the work at hand, the main benefits of a Principal Component Analysis can be summarised as:

1. It quantifies the variance in the data set along different linearly-independent Eigenvectors, yielding insight in the overall information content and distribution of the data

2. Choosing a set of Principal Components, the data set can be reduced in size with a known variance/information loss, allowing easier handling of the data computationally. This benefit is encountered both for the numerical analysis of the data, where high-dimensionality problems can cause problems, as well as that it reduces the overall computational load and therefore computation time

3. PCA may reduce noise in the data set (low variance signals are discarded)

PCA is widely used as a first step in image-analysis and object detection where data sets of many dimensions are studied, such as for facial-, speech- and symbol- recognition, among many others.

Figures 5.1 and 5.2 attempt to exemplify av very simple case of Principal Component analysis of a two-dimensional data set.

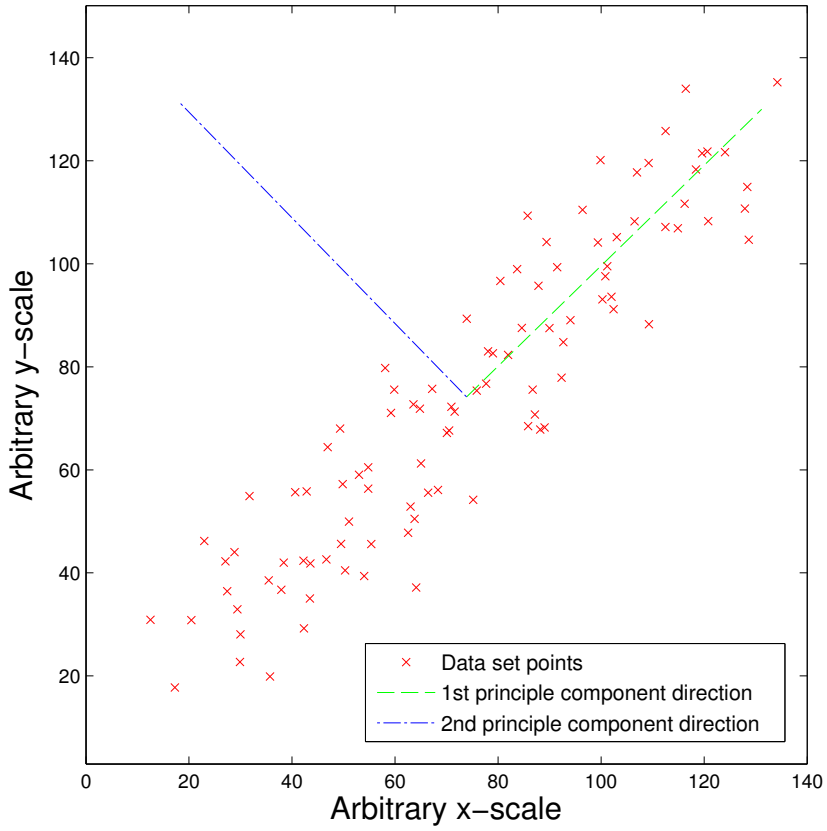

Figure 5.1

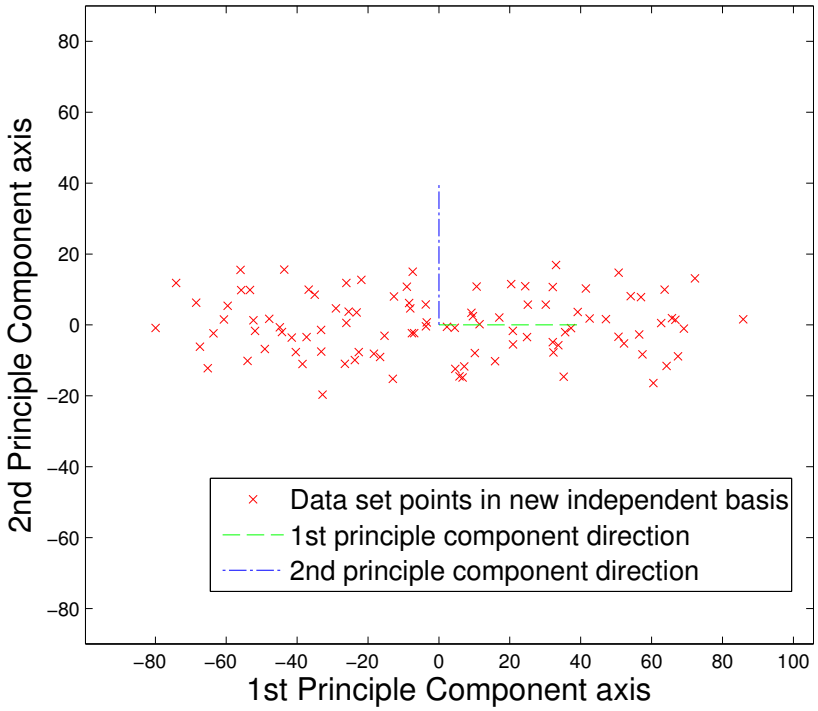

Figure 5.2

In the present context, the PCA performed treats the different intensity values of a single Ca II 8542 Å scan in the data set from the SST as the original variables of the dataset.

The full data set then corresponds to all pixels positions in time and space of the observations. Each data point therefore corresponds to an n-dimensional vector, where n is the number of sampled line-positions in the data set. The observations employ a sampling of $n = 37$ line positions (see Section 3.5), and the original data set is therefore 37-dimensional. As the dimensionality of the observations is therefore rather large, PCA is aptly suited for dimensional reduction to prepare it for further analysis and object-detection using the k-NN-algorithm (see Section 5.4).

5.3.2 Mathematical and Computational implementation of Principle Component Analysis

The main mathematical steps that have to be performed to calculate the Principal Components of a data set, can be summarised as;

1. Calculate the Covariance Matrix of the dataset, detailing the interdependent variance between variables

2. Derive the Eigenvectors and Eigenvalues corresponding to the Covariance Matrix of the data set

3. Sorting the Eigenvectors corresponding to the normalised value of their associated Eigenvalues, largest to smallest, the Principle Components can be selected. The normalised Eigenvalues correspond to the fraction of the total variance that the data along the different Eigenvectors contribute to the data set.

4. Select Principle Components by including Eigenvectors corresponding to a certain fraction of the total variance, e.g. select Eigenvectors so that sufficient variance in the data set is represented (f.ex. so that 90%, 95% or 99% is represented)

The main computational tasks in the above list are steps 1) and 2).

The Covariance matrix of a dataset details the individual covariances between variables. A covariance matrix is therefore a square, symmetrical $n \times n$ matrix, where n is the number of variables in the data set. Element $C(i, j)$ then corresponds to the covariance between variable i and j. Since $C(i, j) = C(j, i)$ (covariances between variables do not depend on their ordering when compared), and $C(i, i)$ is simply the variance of the single variable i, this explains the symmetry of the matrix. The covariance between two variables X_i and X_j in a data set of n data points is generally given as

$$C(i, j) = \frac{\sum_{k=1}^{n} \left(X_{i,k} - \overline{X}_i\right)\left(X_{j,k} - \overline{X}_j\right)}{(n-1)} \tag{5.3}$$

This corresponds to the expectation values of $\left(X_{i,k} - \overline{X}_{i,k}\right)\left(X_{j,k} - \overline{X}_{j,k}\right)$. The value $\overline{X}_i$ simply corresponds to the average, or expected value, of the variable X_i. However, as the average needs to be computed over the entire data set, the simple formula in Equation 5.3 would imply the naive algorithm to compute the covariance matrix:

1. Compute average for all variables $1, 2, \ldots, i, j, \ldots, n$, by $\frac{\sum_{k=1}^{n} X_i}{n}$

2. Compute Covariance Matrix entries for all variables, $C(i, j) = \frac{\sum_{k=1}^{n}\left(X_{i,k}-\overline{X}_i\right)\left(X_{j,k}-\overline{X}_j\right)}{(n-1)}$

This approach is simple, but is both computationally expensive, as it requires two passes through the data set, and may also lead to numerical instability. The instability lies in the danger that the value $\left(X_{i,k} - \overline{X}_i\right)$ for a given $X_{i,k}$ may be very close to zero, and cause numerical imprecision and fatal rounding errors.

The naive algorithm above is therefore preferably replaced with a numerical stable, and less expensive method. A method that meets both these needs is given in Bennet et al. (2009), and is the one employed here. In Bennet et al. (2009), a single-pass approach that ensures numerical stability is presented, and is ideal for large data sets such as the one at hand for the Ca II 8542 Å observations from the SST.

The single-pass algorithm is recursive, calculating successive estimates of $C(i, j)$ and $\overline{X}_i, \overline{X}_j$, updating them throughout the computation.

The implementation of the algorithm discussed is given in Algorithm 1.

for $i = 0;\ i < s;\ i{+}{+}$ **do**
  $\overline{X}_i = 0$
  $\overline{X}_{i,previous} = 0$
  for $j = 0;\ j < s;\ j{+}{+}$ **do**
    $C(i,j) = 0$
    $C(i,j)_{previous} = 0$
  end
end
for $k = 0;\ k < n;\ k{+}{+}$ **do**
  for $i = 0;\ i < s;\ i{+}{+}$ **do**
    $\overline{X}_i = \overline{X}i, previous + (X_i - \overline{X}i, previous)$
    $\overline{X}_{i,previous} = \overline{X}_i$
    for $j = 0;\ j < s;\ j{+}{+}$ **do**
      $C(i,j) = C(i,j)_{previous} + \frac{k-1}{k} \cdot (X_i - \overline{X}_i) * (X_j - \overline{X_j})$
      $C(i,j)_{previous} = C(i,j)$
    end
  end
end

Algorithm 1: Single-pass recursive algorithm for covariance matrix

For an extensive derivation of the recurrence relations in Algorithm 1 above, the reader is directed to Bennet et al. (2009) directly.

After calculating the covariance matrix of the data set, its Eigenvalues and Eigenvectors must be found.

There are many methods to do this and they are widely described, but here the Jacobi-Rotation rotation algorithm, which presupposes a symmetric matrix, is implemented. This algorithm exploits the symmetry of the Covariance matrix, and so is well suited for the problem at hand. The Jacobi-Rotation algorithm is well established, and the reader may study it in Hjorth-jensen (2012) which has a section devoted to it, which the present implementation is based on. The algorithms specifics will otherwise be neglected here.

Using the Jacobi-Rotation algorithm, the Eigenvectors found for the covariance matrix of the data set represent a linearly independent basis along which the associated dataset can be reordered, yielding an informational equivalent dataset to the original, but with uncorrelated variables. Each of the Eigenvectors along which the data set can be ordered also has a specific amount of variance associated with it, that it contributes to the data set. The total variance in the data set is now simply the summed total of the individual variances associated with the different Eigenvectors. The Eigenvalues associated with the different Eigenvectors correspond to the variance associated with the same. Normalising the sum of Eigenvalues to one, each normalised Eigenvalue will correspond to the fraction of variance associated with the corresponding Eigenvector. Hence, selecting a lower bound of variance that must be accounted for in a description of the original data set without losing vital information, a set of Principle Components may be selected. To this end, a number of Eigenvectors are selected such that their combined variance is equal to or greater than the lower bound selected, forming a new basis of fewer dimensions.

The Principle Components should then adequately describe the data set, with a strictly quantified information loss.

5.3.3 PCA performed on the present observations, and selection of Principle Components

The observations used in this thesis are 37-dimensional, with the coordinates being the sampling points in the Ca II 8542 Å -line. For a review of the observations, see Section 3.5. Treating the observations with the PCA analysis as described above, the data set was reordered along 37 new linearly independent coordinates. The corresponding normalised eigenvalues are given in Figure 5.3. The individual normalised eigenvalues correspond to the contribution to the overall variance of their corresponding eigenvectors/dimensions in the data. Sorted by value in the figure, it is apparent that there are a select few eigenvalues that account for most of the variance in the observations, and that many contribute very little.

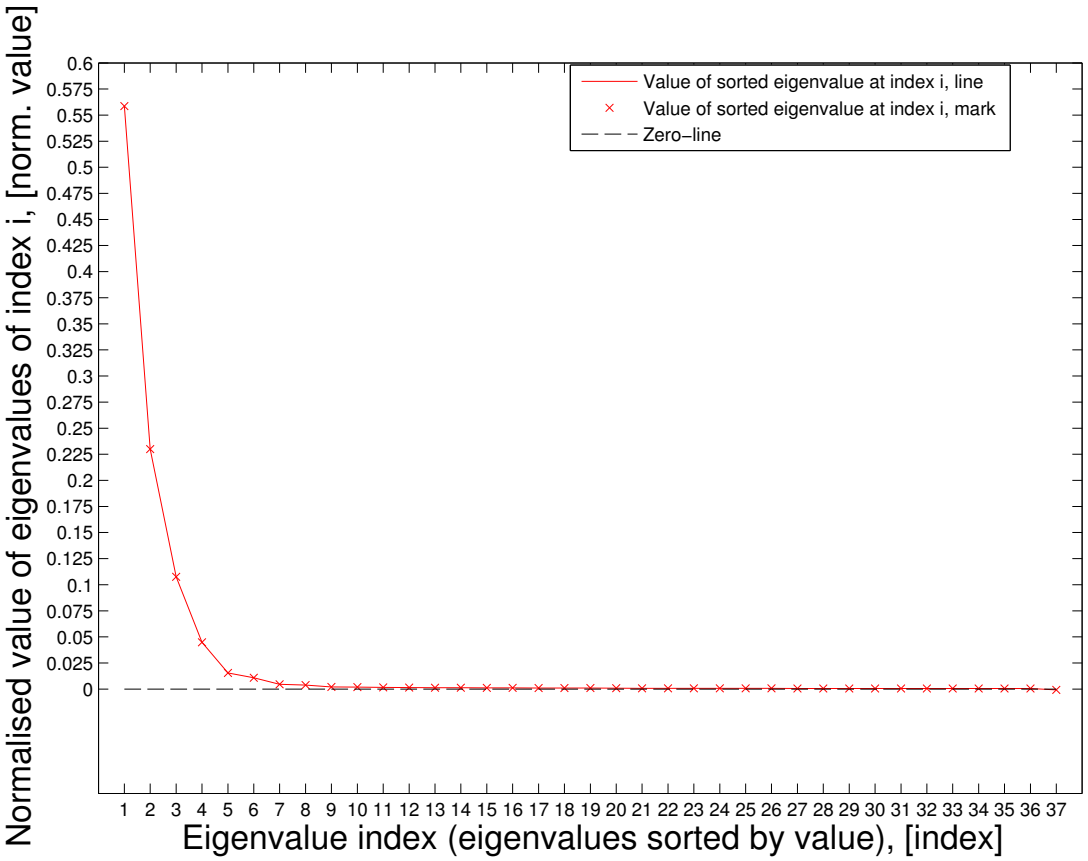

Figure 5.3: Normalised Eigenvalues

The theoretical sum of all variance contributions from the different dimensions/coordinates in the linearly independent new basis is unity. To test that this assertion holds in the practical case of our obser-

vations, the plotted sum of normalised eigenvalues is given in Figure 5.4. From the plot we see that the actual summation goes towards unity, as expected.

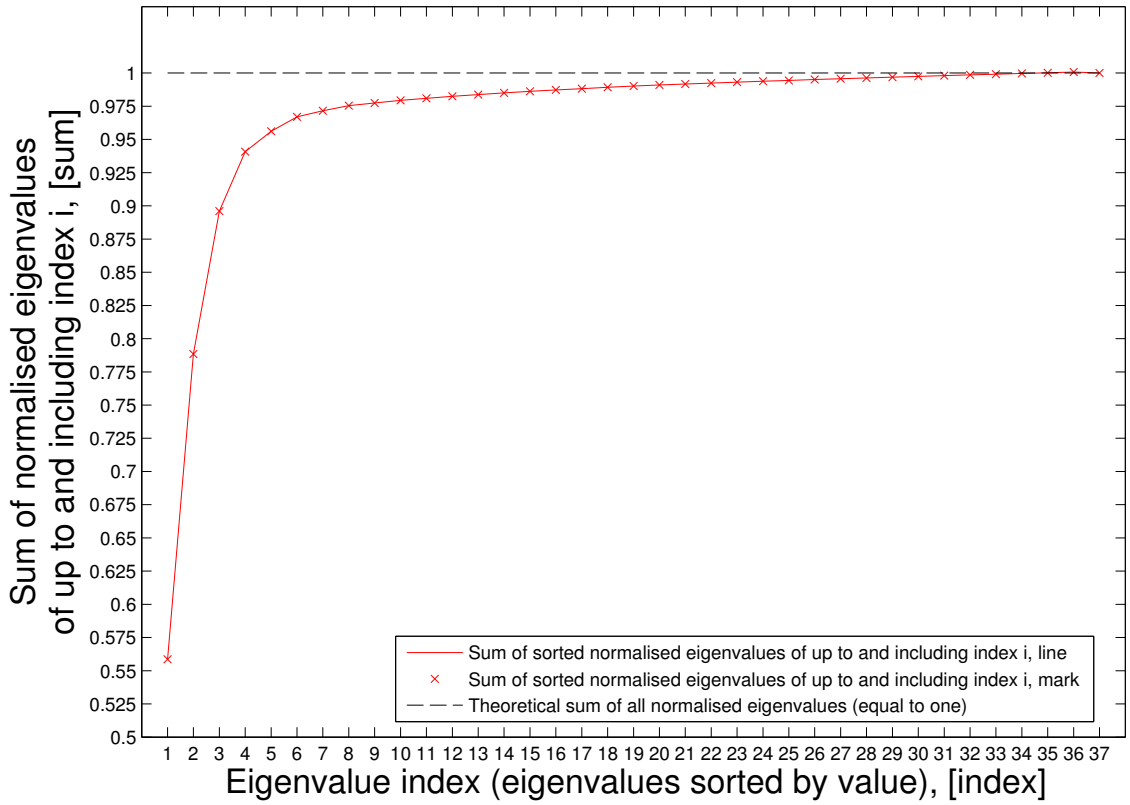

Figure 5.4: Sum of Normalised Eigenvalues

The accompanying values of the summation in Figure 5.4, are given in Table 5.1.

Table 5.1: Summed values of sorted eigenvalues, incrementally adding more eigenvalues of lower values

Nr. of Eigenvalues	Sum of eigenvalues	Nr. of Eigenvalues	Sum of eigenvalues
1	0.5586	20	0.9910
2	0.7885	21	0.9917
3	0.8960	22	0.9925
4	0.9408	23	0.9932
5	0.9562	24	0.9938
6	0.9671	25	0.9945
7	0.9716	26	0.9951
8	0.9754	27	0.9957
9	0.9775	28	0.9963
10	0.9794	29	0.9969
11	0.9810	30	0.9975
12	0.9825	31	0.9980
13	0.9838	32	0.9986
14	0.9850	33	0.9991
15	0.9862	34	0.9997
16	0.9873	35	1.0002
17	0.9883	36	1.0007
18	0.9893	37	1.0000
19	0.9902		

The attentive reader will note that three sums in Table 5.1 are in fact equal to unity or slightly greater than unity (the three last entries). This is of course a deviation from the ideal theoretic foundation of PCA. This effect is due to a small non-positive computed eigenvalue, which in fact can be seen in Figure 5.3 (the last eigenvalue). The computation of a non-positive eigenvalue can pose serious problems and indicate a mischaracterization of the posed problem if its value has significant magnitude. However, in the present context this non-positive eigenvalue has a value after normalisation of $e = -0.000747$. This corresponds to only 0.13% in absolute value of the largest normalised eigenvalue, and can thus be disregarded as negligible.

Selecting the Principal Components for the observations at hand, it was determined that a number of 7 dimensions, corresponding to the first 7 sorted normalised eigenvalues was sufficient to describe the dataset sufficiently well. These 7 dimensions correspond to 97% of the total variance in the dataset, as can be read from the table above.

Example images of the PCA reduced primary observations for a single time frame for these 7 coordinates are given in Figures 5.5 and 5.6.

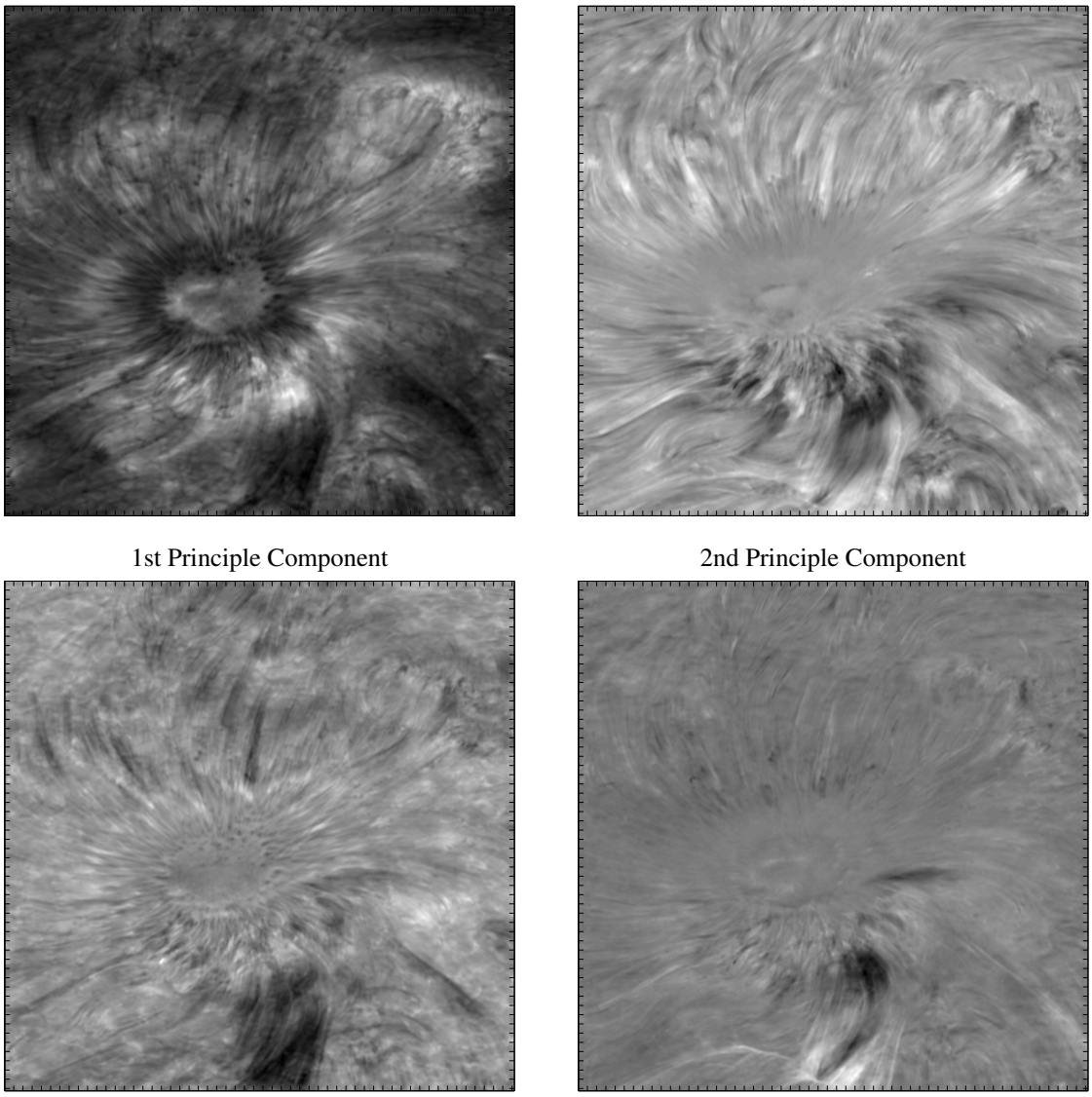

1st Principle Component

2nd Principle Component

3rd Principle Component

4th Principle Component

Figure 5.5: Different example images for the same time frame of the 7 Principal Components for the primary observations. Tick-mark separation is 1".

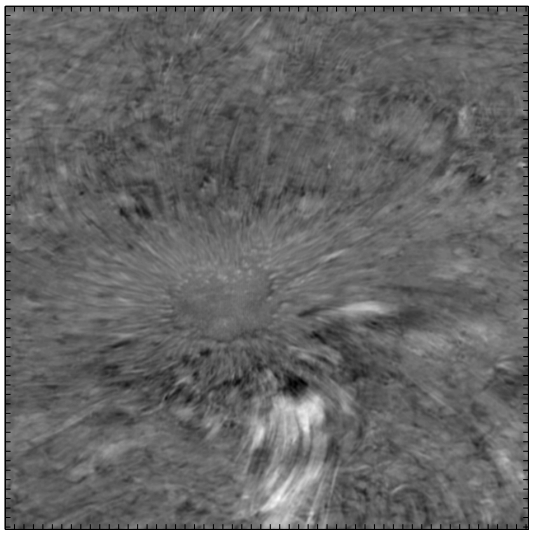

5th Principle Component

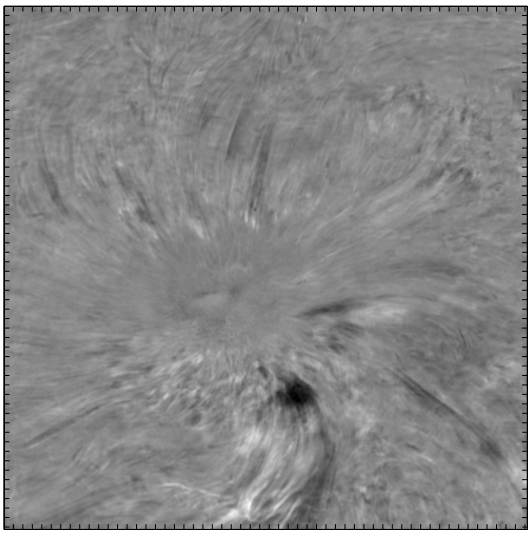

6th Principle Component

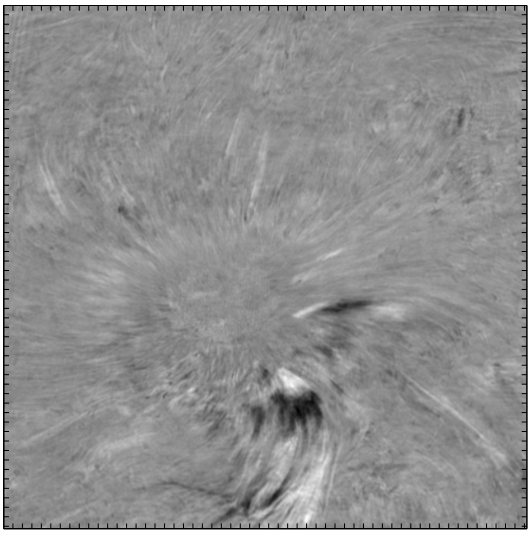

7th Principle Component

Figure 5.6: Different example images for the same time frame of the 7 Principal Components for the primary observations. Tick-mark separation is 1".

5.4 The k-Nearest Neighbour Algorithm

The k-Nearest Neighbour algorithm is a classification algorithm based on a simple comparative approach. It compares vectors from a data set with those in a reference set which have been pre- classified as either

objects (in this present context: PMJs) or non-objects (in the present context this means the quiet sun, penumbra, umbra etc).

The reference set is often a subset of the unclassified data set that has been somehow (usually manually) classified separately. The algorithm passes over each point in the dataset that is to be classified, and compares it to all points in the reference set, and determines the k-nearest neighbours, or k-most-similar points. Similarity can be defined in several ways, but the most common is the euclidean distance between points (if the points also have categorical variables, this would have to be dealt with differently), and this measure is also employed here (with one caveat, see below). After comparing a point to all reference points, and the k-nearest neighbours are established, these neighbours are then polled as to their classification, and the majority determines the classification of the point.

This means points are simply assumed to be of the same type as its nearest neighbours, which is a simple, yet surprisingly effective method. To avoid bias and misclassification, it is essential that varied reference set is assembled, giving a good spread of objects and non-objects spanning the breadth of both their variability (see Section 5.4.2 below). The parameter k is usually taken as a rather small odd number, usually $3 - 7$. The impact of k should be studied and checked for the data set at hand (see Section 5.4.3).

5.4.1 Implementation of the k-NN algorithm

The actual execution of the k-NN algorithm following the successful selection of a suitable reference set is performed as outlined below.

1. Select point in dataset to be classified

2. Compare / calculate distance to all points in the reference set

3. Sort the reference points in increasing order of distance to the point to be classified

4. Select the k- nearest neighbours (k reference points of shortest distance), and determine what the majority of these are classified as - then classify the point according to the majority vote.

5. Repeat for all points in the data set

Figure 5.7 exemplifies how a point is classified in the case of two dimensions.

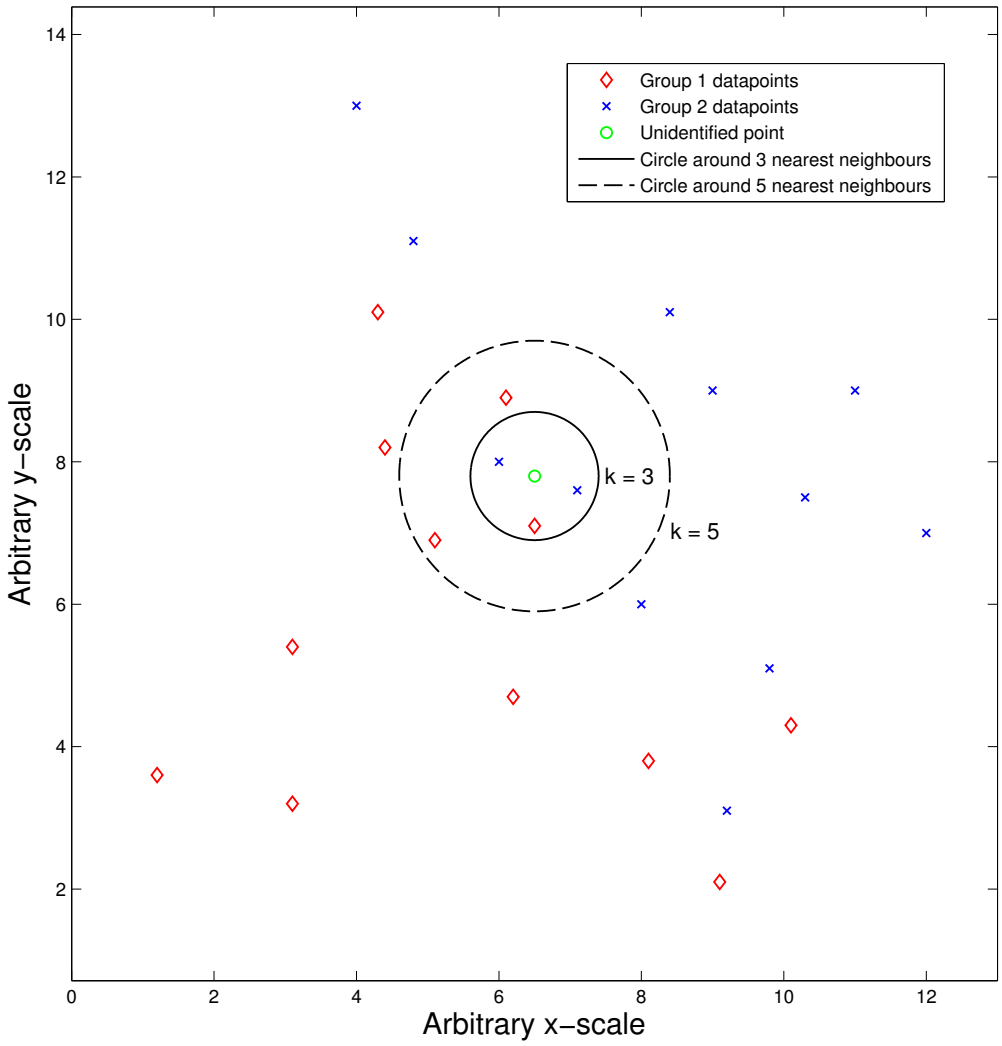

Figure 5.7

5.4.2 Reference set assembly

The k-NN algorithm is very straightforward to implement. However, before the code can be used for detections, a reference set must be assembled. This reference set will consist of a collection of data-vectors drawn from the data to be classified. The reference set is therefore a subset of the unclassified data of interest. This subset is however manually selected and then classified before classification of the entire data set, and used as a means of comparison to the remaining (much more numerous) unidentified data points.

In the present context the data points correspond to the vectors in the multi-dimensional observations after normalisation (see Section 5.2) and the subsequent PCA treatment and dimensionality reduction (see Section 5.3).

In practise, the reference set is selected manually by going through the original 37-dimensional observations and "detecting" PMJs by eye. Also selected is a suitably large and varied sample of non-PMJ positions. The pixel-positions and time frames for the PMJs and non-PMJs are then noted and saved. The by-eye detections are performed using the tool CRISPEX (Vissers & Rouppe van der Voort 2012), which allows easy inspection of multi-spectral observations produced by the Swedish 1-m Solar Telescope's CRISP instrument (see Section 3.5 and Section 3.1 respectively). The PMJ pixel-positions are then used to extract the actual data vectors from the reduced data set and these are saved to the reference set.

It is vital that the resulting reference set spans a wide enough variety of PMJs and non-PMJs data points to ease classification and avoid misclassification. On the other hand, it is also important not to be too liberal in the inclusion of data points as PMJs, as not to have an ill-defined group of objects that will not have a distinct profile in the observations/ data set.

One of the greatest possible biases of the work at hand was just mentioned above; the initial selection of PMJs for inclusion in the reference set. This selection necessitates the same introduction of bias as any manual detection of objects in a data set, and to a large degree defines the object and its characteristics. After the initial selection of objects/PMJs, this subset is then used to find events/objects similar in the metric used - in this case the reduced intensity values in the sampled wavelength (with the caveat that other criteria are introduced later as well, such as minimum size and lifetimes, see Section 5.5). However, as the further selection of new objects to include in the subset of PMJ objects drawn from the data set is now performed by automation, these subsequent classifications should in principle avoid the continuation of this bias in the following detections. Of course, if the initial bias resulting from the selection of the reference set is large enough, the subsequent detections will be futile. It is therefore important to have a clear rule of inclusion in this initial set as to avoid this inevitable bias to cause an ill-posed problem, leading to the automated detections by the k-NN algorithm to become arbitrary. The objects initially selected must also be varied enough as to span the breadth of expected variability in the objects' properties, so as not to exclude desired objects from detections, so that the detections are not too restricted, and consequently again useless.

Figure 5.8 displays all the profiles of the manually selected PMJs included in the reference set, together with their collective average profile, and the overall profile over the entire observations.

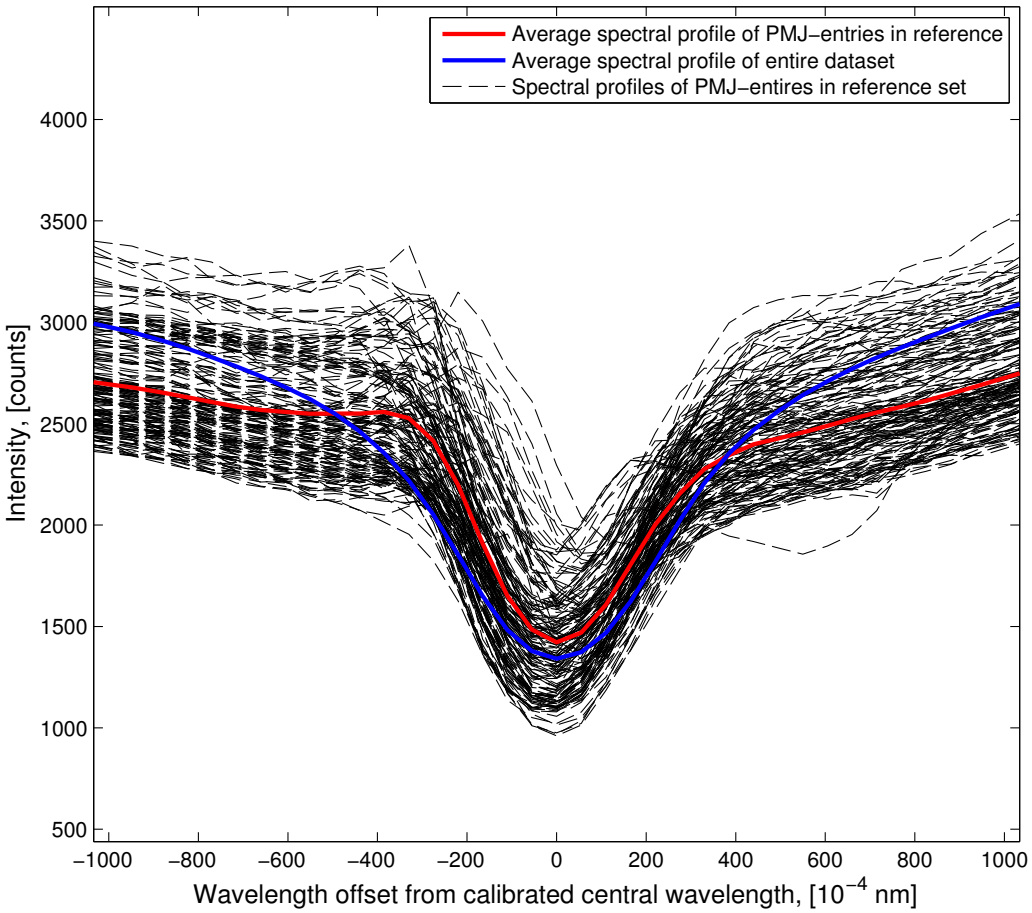

Figure 5.8: The assembled PMJ profiles in the reference set, together with their average profile, and the average profile of the entire observations.

The plot of the average profile already displays a rather clear and recognizable shape, and an analysis of this profile would constitute a result in its own right. However, such an analysis is reserved for the final PMJ profile obtained after k-NN classifcation, and as such is presented in Chapter 6.

5.4.3 k-selection for the k-NN algorithm

To test the accuracy of the k-NN algorithm and to be able to select a suitable value for the parameter k, a cross-test between pre-classified datasets should be performed. To this end, the assembled main reference set is usually split into at least two parts. These constituent parts are then alternately run against each other using the k-NN algorithm using different values for k. This means that one feigns ignorance of the fact that the entries in one of the reference sets is already classified, using the other to reclassify the entries

Table 5.2: Reference set properties

Number of total entries	958
Number of total non-PMJ entries	790
Number of total PMJ entries	168
Number of separate PMJ events contained	55

in it. After this is done, the preclassifications can be compared with the new classifications to establish accuracy estimates, and to determine which value of k maximises the accuracy and minimises the number of misidentifications.

In the present context it was found that a value of $k = 3$ seemed to yield slightly better accuracies than other values in this range.

5.5 Object tracking and statistical analysis

After objects have been classified, the resulting binary images for each time frame must analysed and objects separated, labelled and tracked through time. This is combined with values extracted from images at specific spectral positions in the dataset.

General overview of the object tracking and statistical analysis:

1. Identify discrete connected regions classified as objects/PMJs for each time step. This is in this instance performed using 8-pixel connectivity.

2. Limit objects to connected regions with pixel-areas above a certain threshold, to remove noise/misidentifications of small size in all time steps.

3. Perform an initial labelling of the remaining objects for each time step in the data. Also compute their associated 'Center of Masses' (central pixel of object area), the associated axes of the ellipse with the same second central moments of the object and save the pixel-boundaries and pixel-areas of the objects. These initial associated values can now be used for further restricting the analysis to objects of interest (in the correct area, e.g. the penumbra), and to remove further undesirable objects.

4. Loop through all time steps in the classification data, tracking objects through time. This is achieved by comparing the positions of initially labelled objects across adjacent time steps, selecting the closest objects. The associated distances are then checked against a threshold, if below, they are considered to be the same objects, separated by one time step. Thus, all objects are matched through time, and a library of objects through time established.

   For each time step and for all initially labelled objects, associated properties are also computed. These include the fitted ellipse information of the object (including the orientation of the ellipse), their pixel center of masses, and area -/borders-pixels, and the distance from the pre-defined sunspot-center. These values are appended to the relevant newly-labelled objects that are now tracked

through time. Secondary properties such as 'frame-presence' for each time step and object lifetimes are also updated and incremented.

A not directly associated property also computed for each time step is the fibril direction at Center of Mass of the objects. The fibril directions are computed at several line positions. This is achieved by computing the gradient image of a multi frame running average for each line position, followed by the application of an edge-detection. The detected edges are then used to approximate the local fibril-vector, which is saved. The fibril vectors in the different line positions are then compared with the major-axis of the associated objects, and the angles between them are found.

5. After all objects are matched through time, a last loop over time is performed to remove undesired objects (these criteria can be varied for different interests). Eccentricity of associated ellipses, distance from sunspot center and largest area through time for an object are useful criteria. Eccentricity is a measure for the elongation of the objects, and suitable to select 'classical' PMJs with jet-like morphology. This constraint can be varied to allow for the investigation of objects classified as PMJs with uncharacteristic shapes. The distance from sunspot center is again used to select established PMJs, and the investigation of classified objects outside the penumbra for further study is again also possible. A second size-restriction is beneficial to remove continuous objects that have some size, but do not exceed a slightly larger size than the very low initial threshold either.

   After object-tracking is complete, a full library of objects with associated properties will have been created. The objects are now labelled, and their existence at different time steps noted. As each object has associated lifetimes, and presence (or non-presence) in each time frame is noted - average lifetimes, and average numbers of objects detected per frame are easily computed. Average angular offsets in the different line positions between fibrils and objects are also readily found.

CHAPTER 6

RESULTS

In this chapter the final results as produced by the final object-tracking and statistical analysis of the PMJ detections are presented and analysed.

First, a general investigation of the reasonability of the detections produced, and an analysis of their appearance with regards to the non-PCA reduced observations is carried out in Section 6.1. Then, the inferred spectral profiles of the detected PMJs is presented in Section 6.2, and their significance discussed.

Following this, Section 6.3 deals with the inferred lifetimes and morphology of PMJs, and the corresponding values and their significance are discussed. The found values are then also compared to the established values from Katsukawa et al. (2007) and Jurčák & Katsukawa (2008), being the only source of comparison. An updated thermal energy for the detected PMJs is also inferred using values for the morphology as found in this work, following the approach in Katsukawa et al. (2007).

Lastly, a discussion of the detection of the PMJs in the Ca II 8542 Å -line with respect to the observations in the Ca II H-line is carried out in Section 6.4. Here, an attempt to correlate PMJ detections in the Ca II 8542 Å -line to events in the co-observations of the Ca II H-line is made, and the findings discussed.

6.1 Appearance and reasonability of detections

Here a basic preliminary discussion on the produced detections is carried out. The discussion is based on the appearance of the detections as overplotted on the observations, and is mostly qualitative in nature.

6.1.1 General discussion of the detections

Figure 6.1 depicts a single time frame in the primary observations in the Ca II 8542 Å -line at an offset from the calibrated line-core of -275mÅ . At this offset PMJs were seen to be most visible in the initial by-eye analysis when assembling the reference set for the k-NN detections (see Section 5.4.2). In the figure, the pixel positions classified as PMJs are outlined, and the Major-Axis of the fitted ellipse of the given PMJs are drawn over the events as well. Also outlined is the earlier defined outer boundary of the penumbra used for limiting the detected events to the area corresponding to the rough outline of the

penumbra as observed in the far line wing of the Ca II 8542 Å -line, e.g. the photosphere (see Section 5.5).

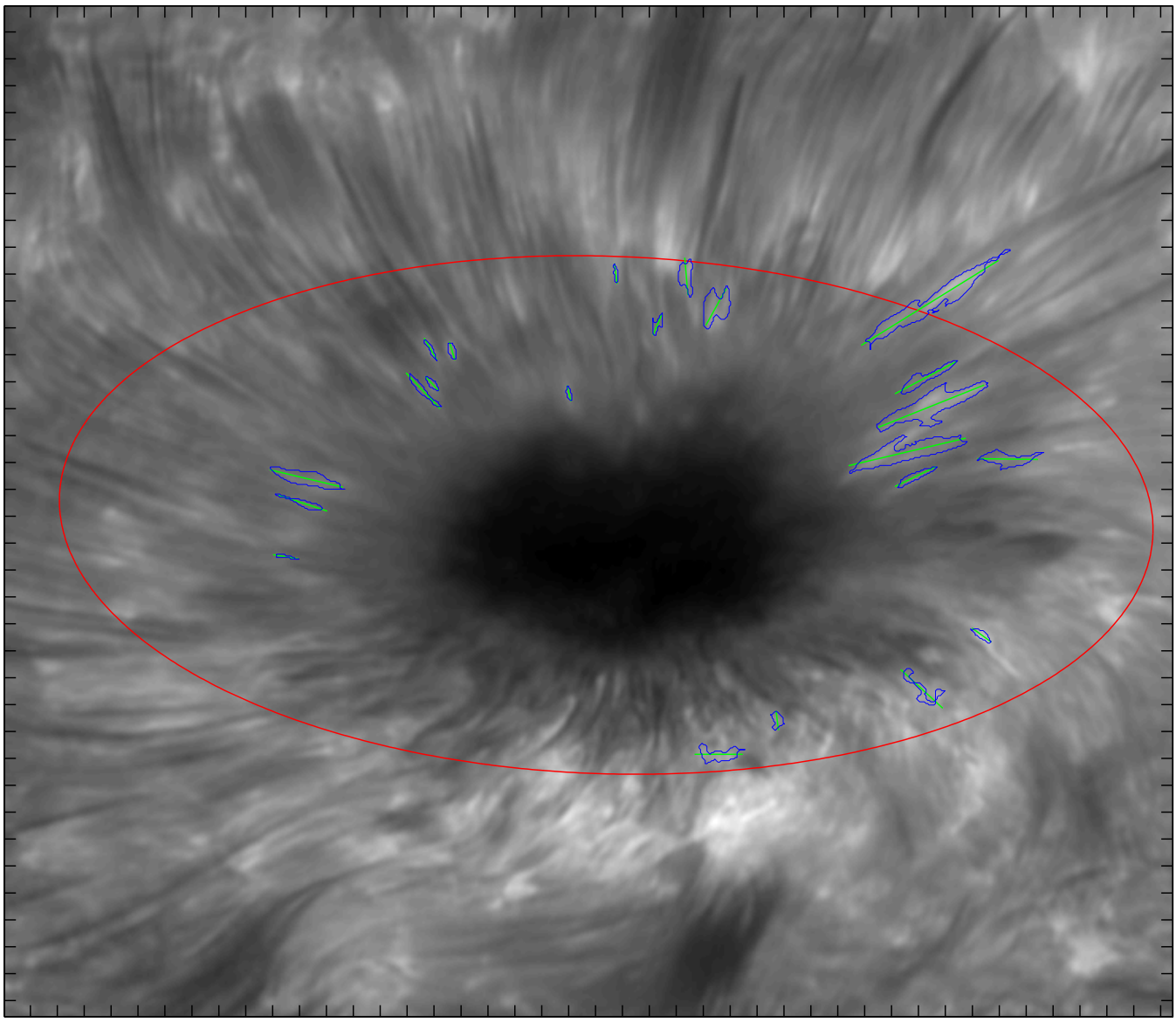

Figure 6.1: Example frame (nr. 113) of PMJ detections , overlain on image at offset of −275 mÅ from calibrated line center at 8541.6 Å. Tick-marks correspond to one arcsecond.

Inspecting the image in Figure 6.1 and the PMJ classified areas, the detection scheme seems to produce reasonable end-results at a first glance. The strongest relative brightenings in the penumbra of the sunspot,

that by eye seem to indicate PMJ-events, are classified as PMJs as expected. Specifically, the events to the upper right of the penumbra that show significant brightening in comparison to their surroundings are well-traced by the k-NN algorithm, and seem to be properly identified. There are also several smaller events in the upward and leftward parts of the penumbra that seem to be correctly identified.

The overplotted major-axes of the fitted ellipses used in the statistical selection process and for attaining measures of the PMJ sizes are also useful as an by-eye check of the orientations of the PMJs. From the example image it seems that the orientation of the PMJs traces the underlying fibril directions of the penumbra to some degree. This would be expected for PMJs, as corresponding to the slight but not extreme offsets of PMJs and their surrounding fibrils as reported in Katsukawa et al. (2007) and Jurčák & Katsukawa (2008).

In the lower right of the image however, there are several classifications of events of dubious validity. These classifications are of both questionable shape and have unusual orientations (especially the lowermost detection in the image, which is near-perpendicular to the fibril direction as seen by eye).

Classifications in this area of the sunspot appear throughout the timeseries, and are in fact quite stable in position, and as such are liable to lead to object classifications with very long lifetimes (this will also be discussed further in Section 6.3). Upon further investigation, these classifications may in part be due to an inflow of matter at this position of the sunspot. This inflow leads to erratic line-profiles which are both irregular in shape and with red-shifted line-cores. Pre-empting the discussion in Section 6.2 somewhat, it is necessary to mention that PMJs have a marked intensity peak in the blue wing of the Ca II 8542 Å -line in comparison to its far wings (as was also noted in the preliminary average PMJ profile as extracted from the reference set established for the k-NN algorithm, Section 5.4.2). As inflowing matter will cause a red-shift in the relevant spectral profiles of the material, this can cause an increase at the vital sampling positions of the Ca II 8542 Å -line as recorded by the SST. This is due to the fact that the wings of the average Ca II 8542 Å -line profile have on average a greater intensity than the wings of the PMJ profile. Shifting the blue wings of these profiles towards the red, may therefore cause a false PMJ-like intensity peak at these sampling positions.

Caution must however be advised to discard these described classification as false-positive all-together. The lower side of the images in the observations corresponds to the observer-side of the sunspot, which implies that the lower half of the spot will exhibit the most severe cases of foreshortening, as the PMJs may be expected to align somewhat with the near-horizontal penumbra. As a consequence PMJs may be so foreshortened that their top-down viewed jet-like appearance is masked, and that they will not have well-defined directions pointing outward from the umbra.

In these considerations it must be kept in mind however that a single time frame is not a valid measure of validity of the classifications. This is both true due to the fact that single frame cannot represent the entire set of classifications, and also because the events studied are events in time as well as in space. The selection criteria as outlined in Section 5.5 specifically include a criteria of connectivity over at least two consecutive time frames for the raw classifications before inclusion in the final set of events classified. To convince oneself of a by-eye validity based on the overplotting of detected objects on the observations, a video is the best way. A timeseries of the detections over the entire range of observations is available online, at URL, and the reader is directed there for further intuitive validity assurances.

6.1.2 The Halo effect

An effect that is both interesting as well as having potential confounding effects on estimated lifetimes as well as morphologies is an effect here dubbed the "halo" effect. The effect is quite apparent when inspecting object classifications and comparing them with the "expected outline" of objects, and the actually produced outlines by the detection scheme.

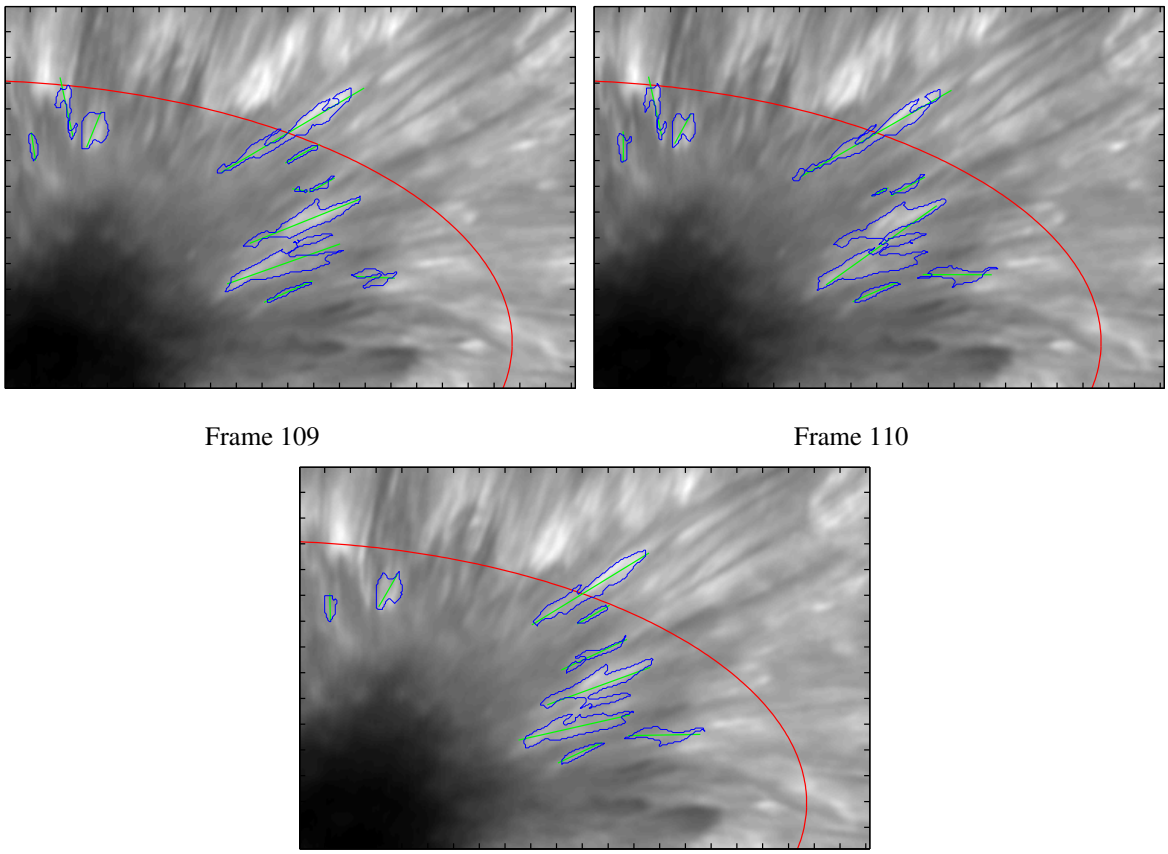

Frame 109 Frame 110

Frame 111

Figure 6.2: Subfield of the full FOV at −275 mÅ from calibrated line center at 8541.6 Å, for three different consecutive time frames. Tick-mark separation is one arcsecond. Note the "halo" described in the text for the detected PMJ events outlined. Furthermore, note the merging of two previously separate PMJ events into one detected object due this effect in Frame 110.

In many cases, the outline around objects is very generous. This is meant in the sense that the object includes quite a large area surrounding the "actual" event as one might have defined it by eye. This halo effect arises from the fact that the classifications of PMJs is ultimately based on recognising the shape of their spectral profiles, and not the intensity of the area to be classified in relation to the surrounding

material. This effect is exemplified in the three time frames given in Figure 6.2.

The effect is especially visible in the second-left-most event in Frame 111 in the figure, which may well have been classified as two separate events by eye.

Furthermore, the two large events to the right of the images in the 1st and 3rd frame are seen to merge in the 2nd frame. This can be explained by positing that as the PMJs reach full size and intensity, their surrounding halos will overlap, and correspondingly become classified as one object. This will be a source for errors in lifetime and size estimations if only "classical" PMJs are to be considered that would not include the halo in their classification as these are not readily visible by eye. Classical here means PMJs as one would detect by eye.

Shortly summarised: the halo effect most likely arises from the fact that the detection scheme attempts to classify by the *shape* of the spectral profile, and not relative intensities. This way, events that may have rather low intensities are still picked out, even though they may have been discarded when employing by-eye detections or some kind of intensity-thresholding-scheme.

The halo effect described above may also contribute to an overestimation of the lifetimes of events, not just contribute to an error in the size estimations. This is due to the fact that many PMJs as investigated in the detections will exhibit halos for quite some time before and after their apparent peak-intensity is reached. Therefore, PMJ detections will be able to overlap more easily not only in space, but also across consecutive time frames. This effect of overlap through time is also strengthened by the fact that some areas in the sunspot observed are prone to production of many PMJs through time, in a cycle of PMJ appearance and waning repeating itself through the timeseries. This is especially quite apparent when the detections are watched overlain on the observations as a video (again, see video of detections at URL).

6.2 The line profile of PMJs in the Ca II 8542 Å -line

As an initial example of the resultant spectral profiles that are inferred for each time frame in the detections, Figure 6.3 depicts the spectral profiles of the PMJs detected in frame 113 in the observations (same frame as for Figure 6.1. The profiles shown correspond to the center-of-mass pixel positions of each separate PMJ event in the frame as output by the classification scheme. Also shown is the average profile of the PMJ detections of that single frame, as well as the average spectral profile over the entire FOV of the observations over *all* time frames (e.g. the average line profile).

A quick inspection of the line profiles presented for the PMJs included in the reference set for the execution of the k-NN algorithm (Section 5.4.2) shows that the the profiles are very similar. This is of course to be expected, as the profiles in the reference set are used to detect the profiles given in Figure 6.3.

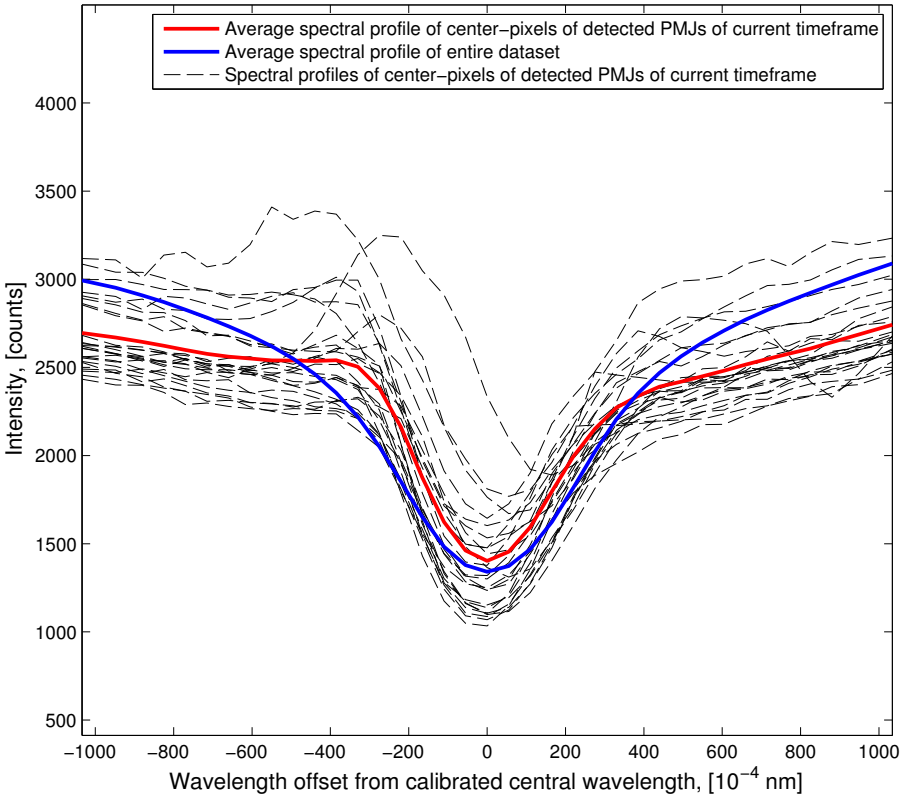

Figure 6.3: Example center-pixel profiles for detected PMJs for one time frame (frame 113), together with their average profile, and the average profile over the whole observation series.

One of the main goals of the thesis was to find the overall PMJ profile in the Ca II 8542 Å -line in the observations at hand. This result is here presented in the form of Figure 6.4. The given overall PMJ profile is the result of averaging the line profiles corresponding to all center-of-mass pixel positions for all final detections of PMJ objects throughout the timeseries of the observations. Also shown is again the overall average line profile over all pixel-positions through all time frames of the Ca II 8542 Å -line observations.

As for the individual time frame average in Figure 6.3, the overall average profile is also very close to the one of the reference set, again, as should be expected.

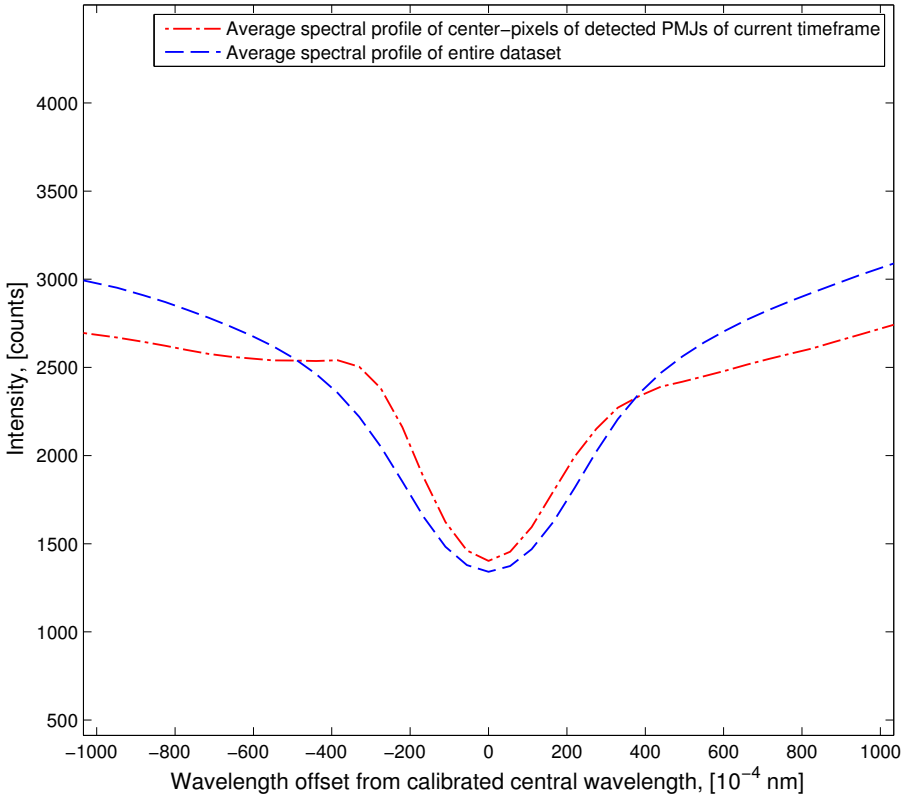

Figure 6.4: Plot of average profile for all detected PMJs and average profile over the whole observation series.

Now in the possession of an overall profile for many detections, the profile can be discussed and described more thoroughly as opposed to the curtailed treatment of the reference set profile in Section 5.4.2.

The final average PMJ line profile is markedly distinct from the full average line profile computed over the full FOV over all time frames of the observations. In itself this implies that the PMJ objects are indeed a distinct class of objects, which are distinguishable by their line profiles.

Furthermore, this indicates that the devised numerical scheme consisting of the Principal Component Analysis, followed by the application of the k-NN algorithm and lastly the numerical object-tracking and selection process was successful in detecting a significant signal based on the assembled reference set.

Both wings of the average PMJ line profile exhibit a markedly lower intensity than the overall average profile of the observations. The line profile further exhibits a distinct peak in the blue wing of the line at an offset of approximately -300 mÅ, followed by slight minimum in the blue wing at an approximate offset of -600 mÅ, and subsequent rise in the far red wing. The red wing of the PMJ line profile is rather flat and does not show a definitive peak like in the blue wing. Still, the red wing's rather straight profile is

still very distinct from the full FOV average profile's red wing, which exhibits a distinct upward curve.

6.3 PMJ lifetimes and morphology

Here the PMJ lifetimes and morphology are first succinctly presented and their statistical significance discussed. Following this, the specific values for the statistics are discussed, and compared to established values in the literature.

6.3.1 Presentation of statistical measures

We begin the section by giving the gathered main statistical values on PMJs in Table 6.1.

The table summarises the inferred average values for all the PMJ event detections. Average values for the average lifetimes are computed from distinct PMJ objects tracked through space and time. Average values for the length and width of the PMJs are calculated from all PMJ events from each frame. The average thermal energy was calculated following the same assumptions as given in Katsukawa et al. (2007) and as reiterated in Section 4.1

Table 6.1: Summary of general PMJ detection statistics

Total nr. of tracked PMJ objects	507
Total nr. of PMJ detections in all frames	5292
Average nr. of PMJ detections	26.2 [events/frame]
Average lifetime of tracked PMJ objects	2.24 [min] (all) or 1.94 [min] (15 min cutoff)
Average length	630.8 [km]
Average width	212.1 [km]
Energy of average PMJ	5.8×10^{15}[J]

The distributions the tabulated values are extracted from are given in histogram plots.

Figure 6.5 and 6.6 display the distribution of PMJ lifetimes, the first for the entire final detected events, the second with a 15 minute upper cutoff. The median and mean values are also indicated in the plots.

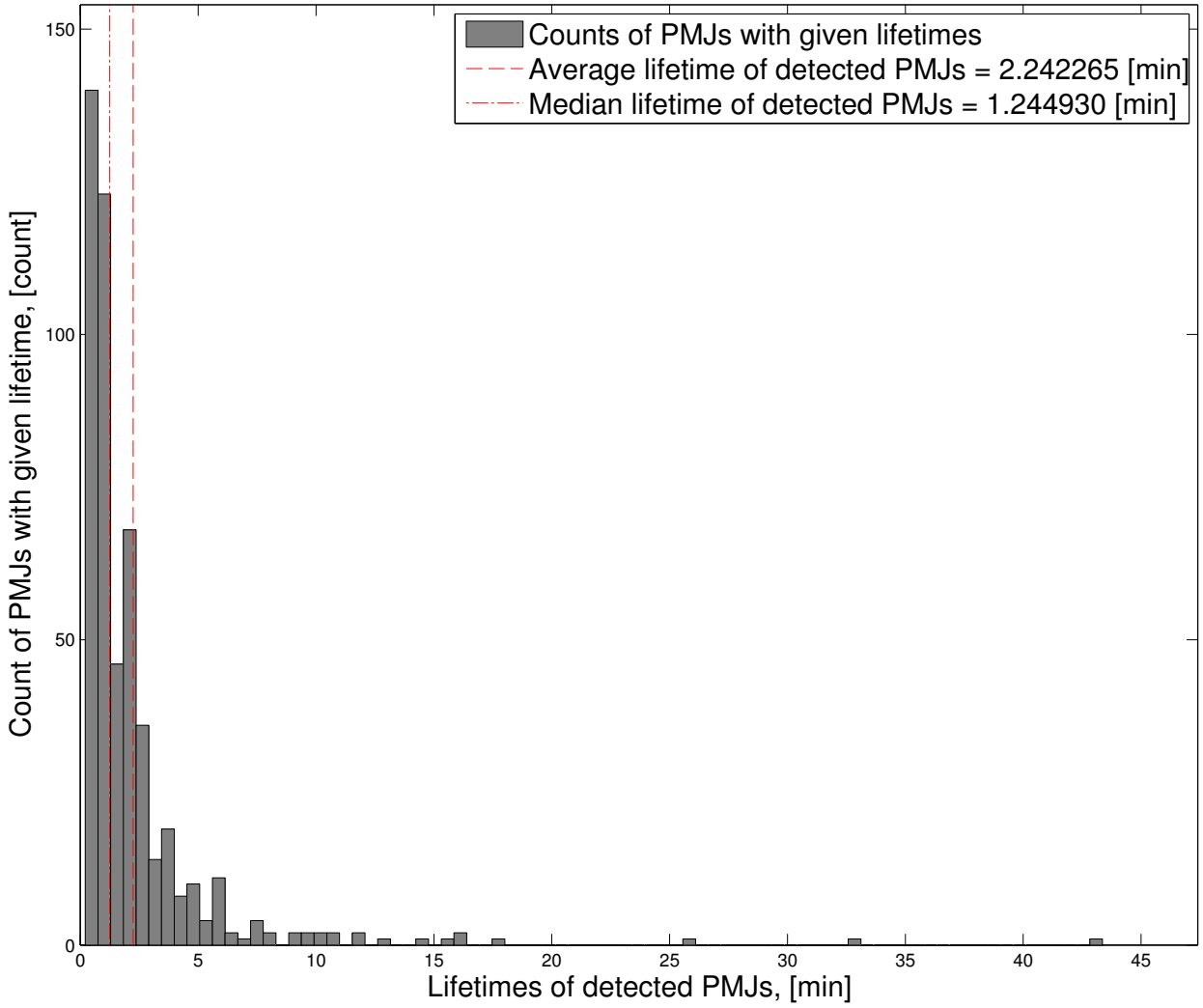

Figure 6.5: Histogram of lifetimes of all detected PMJs throughout the observations.

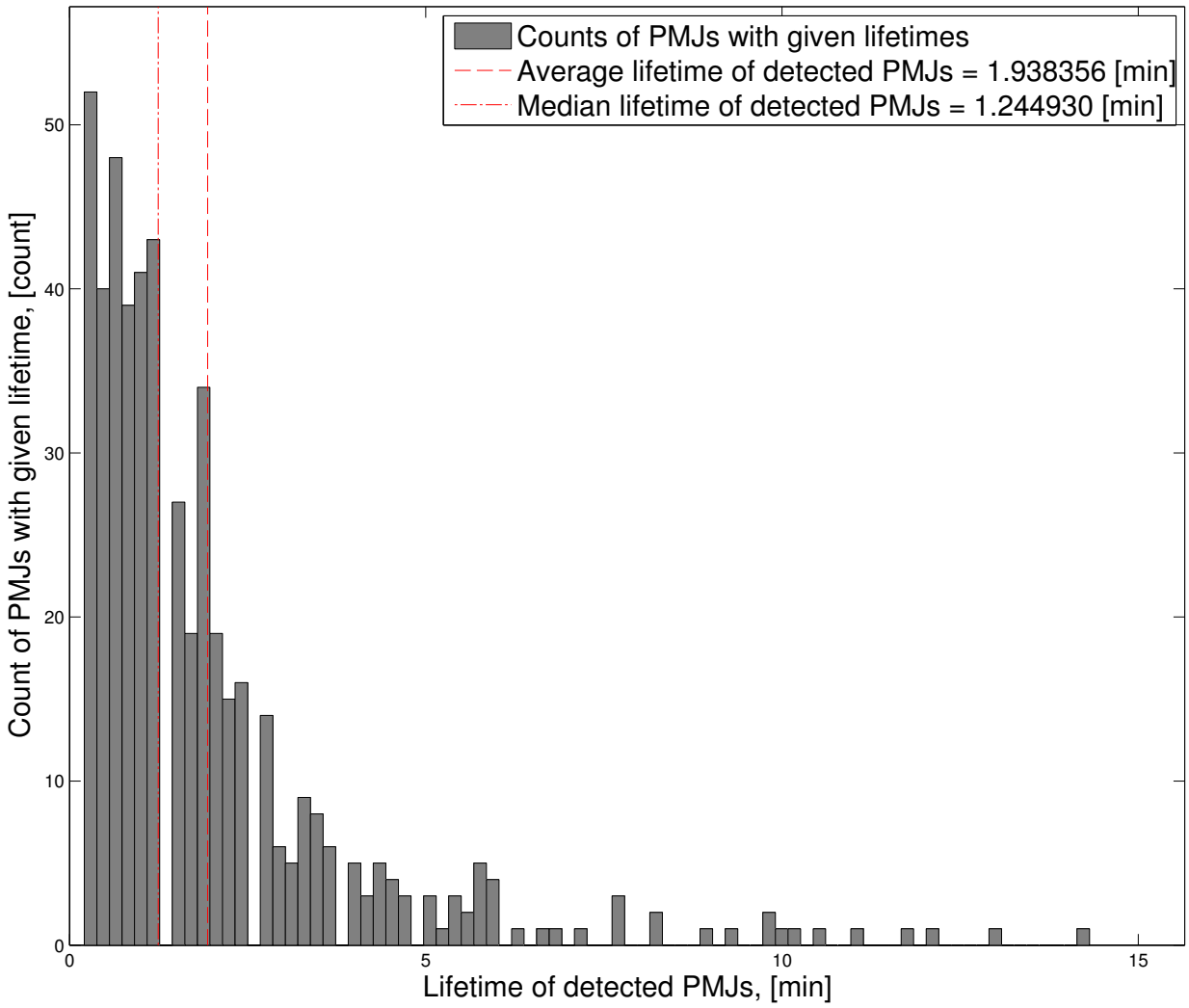

Figure 6.6: Histogram of lifetimes of all detected PMJs throughout the observations, with PMJs with lifetimes over 15 minutes excluded.

Figures 6.7 and 6.8 show the distributions for the PMJ lengths and widths respectively. The entries in the distributions are the PMJs detected in each frame (and not the average length of objects through time - though the means would have been unchanged in any case).

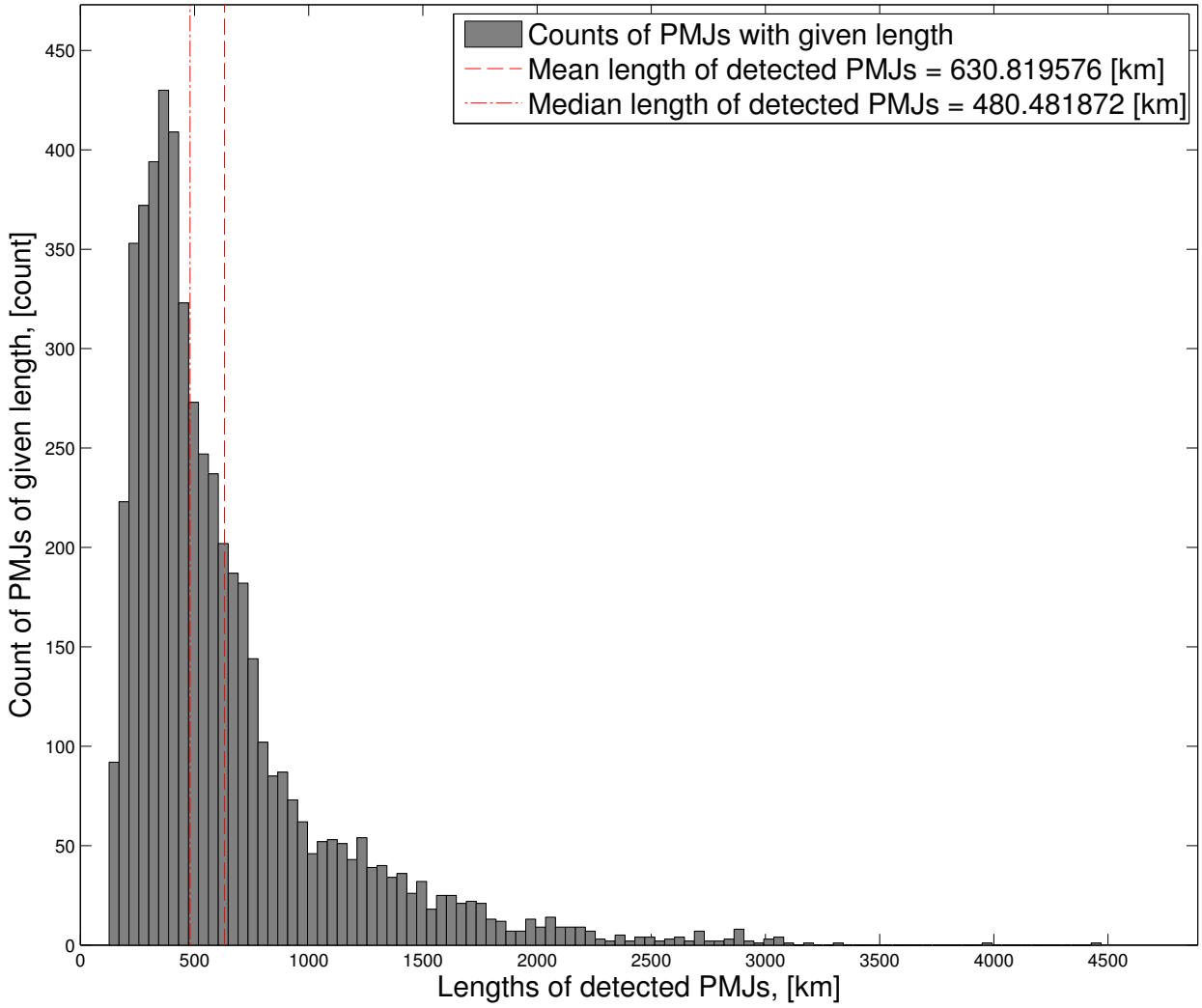

Figure 6.7: Histogram of lengths of all detected PMJs in each frame.

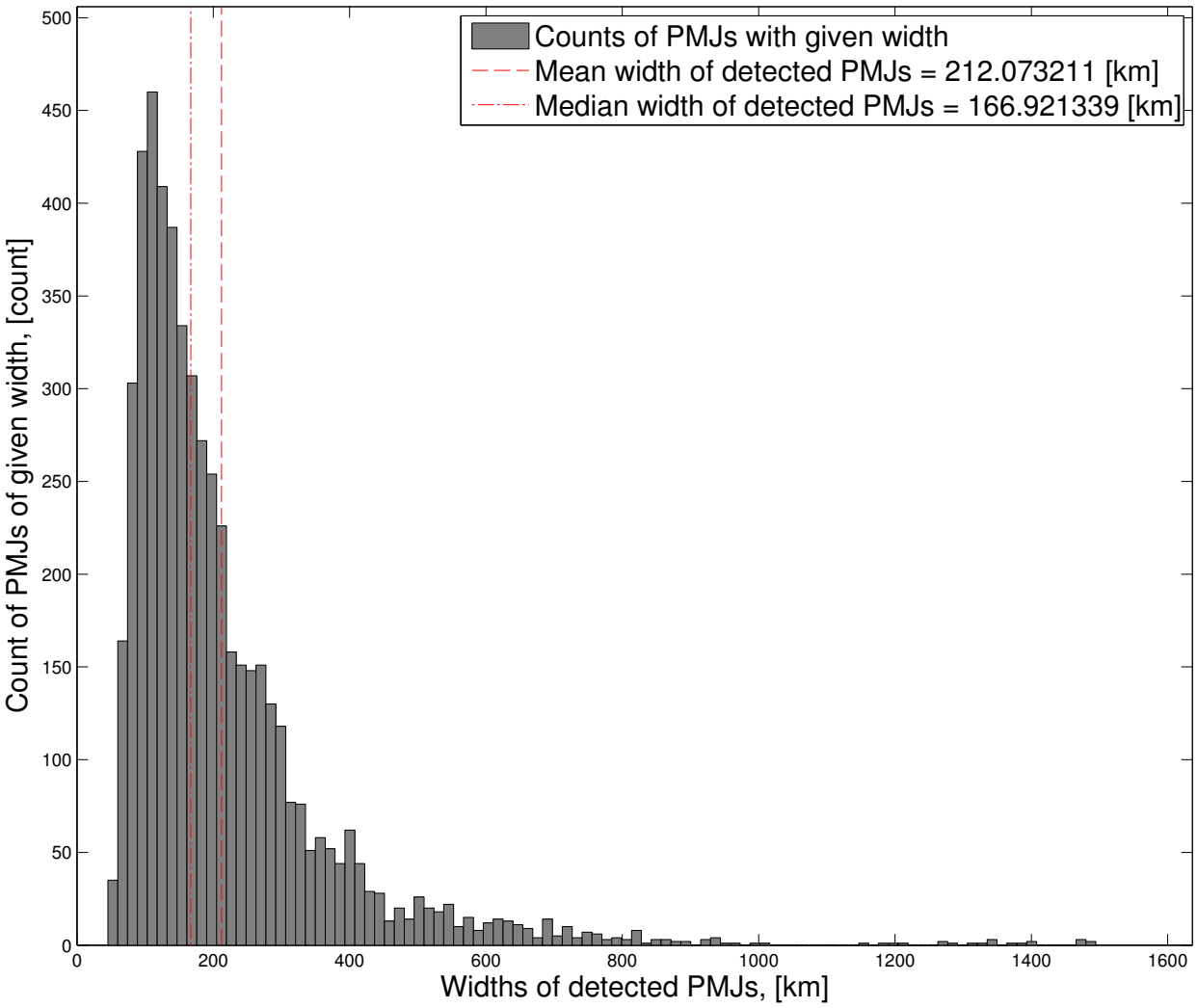

Figure 6.8: Histogram of widths of all detected PMJs in each frame.

The explicit calculation of the thermal energy given in Table 6.1 was carried out by assuming it to be given by the expression $E = \frac{3}{2} n k_b T V$, where n is the number density in the atmosphere, k_b is the Boltzmann constant, T the temperature, and V the volume of the event. Again, assuming the values of $T = 10^4$ K and $n = 10^{18}\text{m}^{-3}$, but this time with the updated volume $V = 630.8$ km $\times (212.1\text{km})^2$. As mentioned, this is the same approach taken and same values assumed as in Katsukawa et al. (2007). This yields the thermal energy for the present average detected PMJ as given in Equation 6.1.

$$E_{\text{Av. PMJ}} = 5.8 \times 10^{15} \text{ J} \tag{6.1}$$

We note that the all histograms seem to correspond to truncated normal distributions. The distributions are necessarily truncated at the y-axis crossings, as negative lifetimes, lengths and widths are nonsensical. The truncation here implies that the calculated means will not directly correspond to the highest-incident position in the given histograms. This is due to the effect readily observable fact that the means lie too close to zero and the distributions are too wide as not to reach the y-axis crossing. A straight-forward normal distribution approximation to the empirical distributions given is therefore not applicable.

6.3.2 Comparison and discussion of found statistical values

While in the expected general magnitudal range, several of the extracted statistical measures on PMJs as presented in Section 6.3.1 evidently differ quite significantly from previously reported values in Katsukawa et al. (2007)and Jurčák & Katsukawa (2008).

For convenience, the relevant values on PMJs characteristics from the literature as summarised in Table 4.1 and the corresponding values found here as given in Table 6.1, are all drawn together in Table 6.2.

Table 6.2: Summary of general PMJ detection statistics

Measure, x	Thesis values	Literature values*	Ratio, $x_{\text{thesis}}/x_{\text{literature}}$	η, relative difference**
Lifetime	1.94 [min]***	1 [min]	1.94	0.93
Length	630.8 [km]	3000 [km]	0.21	0.79
Width	212.1 [km]	350 [km]	0.61	0.39
Energy	5.8×10^{15}[J]	2×10^{16} [J]	0.29	0.71

* Values from Katsukawa et al. (2007) and Jurčák & Katsukawa (2008). Original ranges are listed as their midvalues.

** Definition of the relative difference is given in Equation 6.2.

*** From distribution with 15 minute cutoff

The relative differences tabulated in 6.2 employs the definition of η as given in Equation 6.2 (x is one of the different measures).

$$\eta = \frac{\epsilon}{|x_{\text{literature}}|} = \frac{|x_{\text{literature}} - x_{\text{thesis}}|}{|x_{\text{literature}}|} \tag{6.2}$$

To compare the values from the literature and the here reported values for PMJs, inspecting the ratio between values, and the relative difference between the values can be beneficial.

Discrepancy details

The relative difference serves as a unitless comparison, and measures the absolute ratio of the distance between two values over one of the values as a reference. The literature values as given in Table 6.2 were used as the reference values. We see from the table that the relative differences are quite large. None of the values reach unity, signifying a size in the absolute difference as large as the reference values from the literature, but many are not far off.

In this comparison, the lifetimes considered are those for the distribution with an upper 15 minute cut-off. Inspecting Figures 6.5 and 6.6 we see that for the distribution with no cutoff, we have several outliers that lie to the far right, with lifetimes reaching the overall duration of the observations (42 minutes). These lifetimes are most likely due to persistent misclassifications as mentioned in Section 6.1.1.

The lifetimes presented here are about 1.9 times as long as the ones from the literature. For the lifetimes, this result is not overly worrying. The lifetimes are in both cases in the range of only a few minutes, which can easily lead to large relative differences, as these are such small values.

The ratio between the length reported here and the value from the literatures however, as well as their relative difference, may cause greater concern. The here reported value corresponds to only about 20% of the midvalue in the literature. Also, the relative difference for these is almost 80%, which is a significant difference. In all, the reported lengths are significantly shorter than the ones in the literature.

In the same vain, though not as significantly, the reported values of the widths also come up shorter than the established ones. The ratio and relative difference correspond to about 60% and 40%, which is not as great a deviation as for the length, but still significant.

A point to be made however is that the fact that both the length *and* the width reported here are shorter is more of a reasonable result than if either of them had been very close to the established values and the other not, or if one measure was significantly longer and the other shorter. The fact that their variation is in the same direction for the both of them, is in that sense a positive, as one would intuitively expect both to be effected equally by some systematic difference in the observations or methodology.

The energy for PMJs reported here also has a significant deviation from the earlier reported values. This should already be expected from the length and width consideration however, as the energy expression is proportional to the estimated volume of the PMJs, which in turn is proportional to the length, or alternatively proportional to the square of the width. That the energy reported here therefore is significantly lower than in the literature, only about 30%, is not surprising as a consequence.

Possible causes of discrepancies

All in all, the here reported values are generally lower than those reported in the literature, as detailed above. The values are however not inherently unreasonable, nor are they magnitudes removed from the established values.

Possible causes of the discrepancies observed are many. Differences in viewing angle, a PMJ size dependency on the sunspot location or sunspot properties (such as for example magnetic field strengths) and the properties of the observing instrument may all contribute to the differences observed. Furthermore,

the selection criteria and methods of detecting PMJs in the present context and the previous publications may themselves influence the statistics inferred from these.

A readily mentioned and discussed possible reason for the discrepancies observed is the difference in the employed instruments.

A quickly investigated difference between the SST and the SOT is their resolving power. As the SOT has about half the main aperture size of the SST, 0.5 meters (Tsuneta et al. 2008) vs 0.97 meters (Scharmer et al. 2003a), one may naively assumed that the presented observations in the Ca II 8542 Å -line have a greater resolution than the ones presented in Katsukawa et al. (2007) and Jurčák & Katsukawa (2008).

The theoretical diffraction limits of the SST in both the Ca II 8542 Å -line and the Ca II H-line from Section 3.1.1 are repeated here for convenience in Equations 6.3 and 6.4 respectively. As a comparison, the diffraction limit of the SOT (Tsuneta et al. 2008), which was employed in the previous investigation of PMJs in Katsukawa et al. (2007) and Jurčák & Katsukawa (2008), is given in Equation 6.5.

$$\theta_{\text{SST, Ca II 8542 Å}} = 0.22'' \tag{6.3}$$

$$\theta_{\text{SST, Ca II H-line}} = 0.10'' \tag{6.4}$$

$$\theta_{\text{SOT, Ca II H}} = 0.2'' \tag{6.5}$$

We see that although the SST has a greater theoretical diffraction limited resolution in the same lines as the SOT, that when comparing observations from the SST in the Ca II 8542 Å -line to observation in the Ca II H-line, the diffraction limits are very similar (in fact the SST limit may be slightly larger). We see that in this instance the broadening by the longer wavelength of the Ca II 8542 Å -line is stronger than the benefit granted by the larger aperture of the SST. Thus, expecting differences in size estimations due to diffraction limitations in the SOT observations should not warranted.

Without estimations for the magnetic field-strengths of the sunspot observed both in the observations used here, and the sunspot observed in Katsukawa et al. (2007), an investigation of the dependence of PMJs on their magnetic environment is not feasible. As such, it is not attempted here, as this data is not available. However, as PMJs are assumed to be caused by magnetic reconnection, a connection to the sunspots magnetic field strengths does not seem unreasonable.

Methodology considerations

An important possible reason for the discrepancies in the statistical measures observed that must be discussed are the large differences in methodology in the present work and in Katsukawa et al. (2007) and

Jurčák & Katsukawa (2008).

In this thesis the detection scheme implemented does not assume a given specific size in the PMJs that are to be detected. The detections are performed automatically using a similarity measure that is based on the spectral signature of potential events alone, albeit followed by additional selection criteria pertaining to small minimum sizes and a not too-restrictive shape requirement (see Section 5.5).

The initial spectral signatures selected for the reference set employed by the k-NN algorithm were selected manually, but they were included liberally with regards to shape and size of the objects found by eye, and mostly by shape-selection of the signature (see Section 5.4.2). One can therefore expect that the inferred values of length and widths of the detected PMJs should be rather uninfluenced by the initial selection of the reference set. The selection of reference events did not rely heavily on relative intensities as seen by eye either. As long as events were discernible at all and matched the loose criteria of being relatively short lived and exhibiting a brightening in the wings of the line they could be included in the reference set. The reference set bias is thus most heavily tilted towards selection of events with similar shaped line profiles, but not towards selection by size. In all, this means that the method should not be greatly biased to select PMJs by other criteria than their line profiles. The sample size produced by the method is also large. With a total number of 507 tracked events through time, and a total of 5292 detected PMJs summed over all frames, the statistical measures inferred from the detections can certainly be seen as significant. The plotted distributions of the statistical measures in Section 6.3 do not display unexpected non-clustered or ill-constrained means either, and so underpin the sample validity.

In contrast to the methodology above, the detections presented in Katsukawa et al. (2007) and Jurčák & Katsukawa (2008) are all performed manually. Furthermore, the only selection criteria available were the apparent brightening in the Ca H-line wide band image, their perceived lifetimes and finally their sizes. This means that one of the primary detection criteria used was itself later reported as an inferred value from the detections. Especially the lower and upper limits on size of PMJs will be hard biases to avoid in by-eye detections, as these are inevitably criteria the eye will grow accustomed to. Furthermore, PMJs with larger sizes are evidently easier to see, and may therefore be over-selected for this reason. Additionally, the sample size of events as reported in Jurčák & Katsukawa (2008) has a size of only 209. These detections also seem to be of individual detections in single time frames, not of objects tracked through time (this is not explicitly specified, but assumed here from context). This sample size is therefore to be put in contrast to the reported 5292 events for all time frames presented here.

In conclusion with regards to the observed discrepancies and the differences in methodology in the detection of PMJs, it can be asserted that the presented detection scheme should suffer from less selection bias, as well as possible correlations between any possible bias and the inferred statistical measures, than a simple manual detection scheme. Furthermore, the automated scheme presented and employed here produces a sizeable sample size, with well bounded distributions of the statistical measures. The by-eye detections used in the earlier detections performed in Katsukawa et al. (2007)and Jurčák & Katsukawa (2008) on the other hand may very well suffer from the usual problems accompanying manual detections such as selection bias through familiarity.

6.4 PMJs in the Ca II 8542 Å -line viewed in the Ca II H-line

In this final section a quick look is taken at detections of PMJs in the Ca II 8542 Å -line and if they have visible counterparts in the co-observed Ca II H-line observations (see Section refsec:dataset).

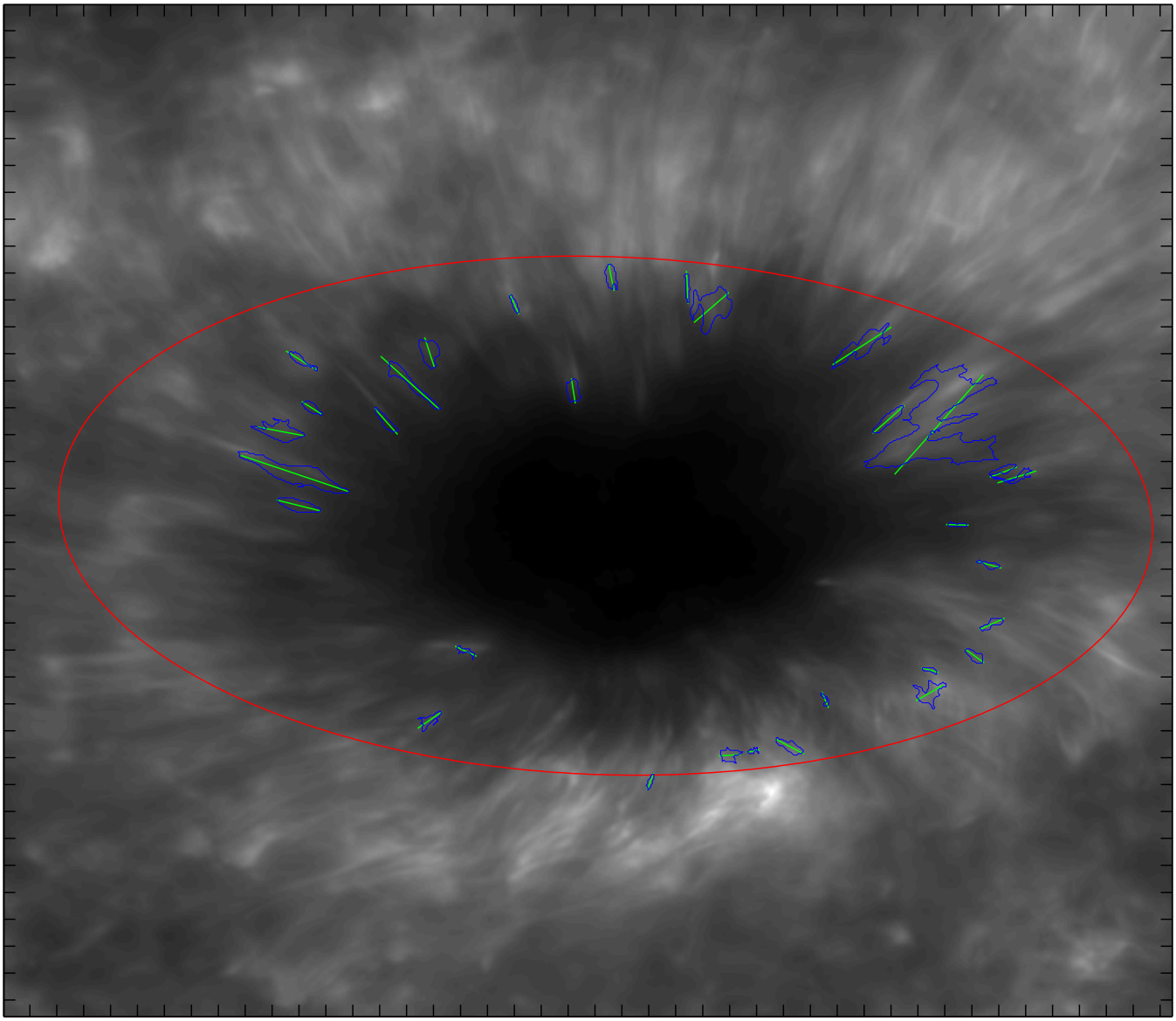

Figure 6.9: Example frame (nr. 99) of PMJ detections, overlain on the Ca II H-line detections co-observed with the Ca II 8542 Å -line observations. Tick-marks correspond to one arcsecond.

Figure 6.9 displays a time frame from the Ca II H-line detections from the SST (see Section 3.5), overlain are detections of PMJs as detected in the Ca II 8542 Å -line observations.

In the image we can readily see that many of the detections performed on the Ca II 8542 Å -line observations have corresponding counterparts in the Ca II H-line. Furthermore, it can be seen that many detections overlapping with bright objects in the Ca II H-line observations do further down the base of the PMJs towards the umbra. This might be an indication of PMJs penetrating further up the atmosphere, and being partially captured further up in the atmosphere by the Ca II H-line, and partially further down in the Ca II 8542 Å -line. This is due to the fact that the Ca II 8542 Å -line has a slightly lower formation height than the Ca II H-line (see Figure 2.1, where the Ca II K-line closely follows the formation height of the Ca II H-line).

A more detailed study would be in order to properly investigate this apparent behaviour.

CHAPTER 7

CONCLUSION AND OUTLOOK

The final results produced and presented in the last chapter are encouraging proof that numerical methods applied on data containing highly resolved line profiles can be used to good effect. The detection of a well defined and statistically significant spectral signature for Penumbral Microjets exemplifies the potential power of detection schemes exploiting the often untapped potential of observations with highly resolved spectral lines, such as produced by the Swedish 1-meter Solar Telescope.

Usage of spectral signatures as a means of detection and classification is also shown to be advantageous as a possible means to avoid selection bias, as the distinct spectral signature of a feature can easier be separated from its other identifiers, thereby avoiding confounding effects between selection criteria and the very properties one wishes to infer from the detections.

Furthermore the thesis is in effect a proof-of-concept of the successful application of widely established high-dimensionality reduction and classifications methods to the field of solar physics. It is the author's opinion that the added complexity of a pipeline spanning Principal Component Analysis, the application of the k-Nearest Neighbour algorithm and the object tracking and statistical treatment is well worth the reaped benefits of an automated numerical scheme that in principle can be applied to a wide variety of solar features with distinct spectral profiles. The automated detections of features also opens avenues to linking features with perhaps differing appearance but with similar spectral signatures.

In the future a more detailed investigation of individual detected PMJs in the large assembled object sample would be interesting. Further, the automated determination of fibril directions surrounding PMJs was begun during the work on this thesis with the intention of using the fibril-PMJ offset values to estimate the inclinations of PMJs for the assembled PMJ sample, as was performed manually for the PMJs described in Jurčák & Katsukawa (2008). The offsets were to be computed for fibril directions in different Ca II 8542 Å -line sample positions in the SST observations, as well as for the secondary Ca II H-line observations in order to link them to the literature.

Unfortunately unawares to the author, a paper on Penumbral Microjet line profiles in the Ca II 8542 Å -line was published before the completion of this thesis, Reardon et al. (2013). This was sadly not realised before incorporating comparisons and discussions of similarities between the results presented here and in Reardon et al. (2013)became infeasible because of time constraints. Rectifying this would be a top priority in future work with the subject matter at hand.

BIBLIOGRAPHY

Bennet, B., Grout, R., Pebay, P., Roe, D., & Thompson, D. 2009, Proceedings of IEEE International Conference on Cluster Computing

Carlsson, M. & Leenaarts, J. 2012, A&A, 539, A39

Carroll, B. & Ostlie, D. 2007, An introduction to modern astrophysics (Pearson Addison-Wesley)

Fried, D. L. 1966, Journal of the Optical Society of America (1917-1983), 56, 1372

Guo, G., wang, H., Bell, D., et al. 2004, in Computational Linguistics and Intelligence Text Processing, 5th International Conference, CICLing 2004, Springer, Seoul, Korea, 559–570

Hjorth-jensen, M. 2012, COMPUTATIONAL PHYSICS, Lecture Notes Fall 2013

Houle, M. E., Kriegel, H.-P., Kröger, P., Schubert, E., & Zimek, A. 2010, in Proceedings of the 22Nd International Conference on Scientific and Statistical Database Management, SSDBM'10 (Berlin, Heidelberg: Springer-Verlag), 482–500

Jurčák, J. & Katsukawa, Y. 2008, A&A, 488, L33

Katsukawa, Y., Berger, T. E., Ichimoto, K., et al. 2007, Science, 318, 1594

Lemen, J. R., Title, A. M., Akin, D. J., et al. 2012, Sol. Phys., 275, 17

Löfdahl, M. G., Henriques, V. M. J., & Kiselman, D. 2011, A&A, 533, A82

Löfdahl, M. G. & Scharmer, G. B. 2012, A&A, 537, A80

Löfdahl, M. G., van Noort, M. J., & Denker, C. 2007, in Modern solar facilities - advanced solar science, ed. F. Kneer, K. G. Puschmann, & A. D. Wittmann, 119

Müller, D. A. N., Schlichenmaier, R., Steiner, O., & Stix, M. 2002, A&A, 393, 305

Nelson, C. J., Doyle, J. G., Erdélyi, R., et al. 2013, Sol. Phys., 283, 307

Reardon, K., Tritschler, A., & Katsukawa, Y. 2013, ApJ, 779, 143

Scharmer, G. B., Bjelksjo, K., Korhonen, T. K., Lindberg, B., & Petterson, B. 2003a, in Society of Photo-Optical Instrumentation Engineers (SPIE) Conference Series, Vol. 4853, Society of Photo-Optical Instrumentation Engineers (SPIE) Conference Series, ed. S. L. Keil & S. V. Avakyan, 341–350

Scharmer, G. B., Dettori, P. M., Lofdahl, M. G., & Shand, M. 2003b, in Society of Photo-Optical Instrumentation Engineers (SPIE) Conference Series, Vol. 4853, Innovative Telescopes and Instrumentation for Solar Astrophysics, ed. S. L. Keil & S. V. Avakyan, 370–380

Scharmer, G. B., Kiselman, D., Löfdahl, M. G., & Rouppe van der Voort, L. H. M. 2003c, in Astronomical Society of the Pacific Conference Series, Vol. 307, Solar Polarization, ed. J. Trujillo-Bueno & J. Sanchez Almeida, 3

Scharmer, G. B., Narayan, G., Hillberg, T., et al. 2008, ApJ, 689, L69

Sekse, D. H. 2013, Doctoral Dissertation

Shine, R. A., Title, A. M., Tarbell, T. D., et al. 1994, ApJ, 430, 413

Shlens, J. 2005, in Systems Neurobiology Laboratory, Salk Institute for Biological Studies

SST Wiki. 2013, CRISP Wiki Entry, last Accessed: 08.05.14

Tsuneta, S., Ichimoto, K., Katsukawa, Y., et al. 2008, Sol. Phys., 249, 167

van Noort, M., Rouppe van der Voort, L., & Löfdahl, M. 2006, in Astronomical Society of the Pacific Conference Series, Vol. 354, Solar MHD Theory and Observations: A High Spatial Resolution Perspective, ed. J. Leibacher, R. F. Stein, & H. Uitenbroek, 55

van Noort, M., Rouppe van der Voort, L., & Löfdahl, M. G. 2005, Sol. Phys., 228, 191

van Noort, M. J. & Rouppe van der Voort, L. H. M. 2008, A&A, 489, 429

Vernazza, J. E., Avrett, E. H., & Loeser, R. 1981, ApJS, 45, 635

Vissers, G. & Rouppe van der Voort, L. 2012, ApJ, 750, 22

Yang, Y. & Liu, X. 1999, in (ACM Press), 42–49